

1
2
3
4
5
6
7
8
9
10
11
12
13
14
15
16
17
18
19
20
21
22
23

Uncertainties of satellite-derived surface skin temperatures in the polar oceans: MODIS, AIRS/AMSU, and AIRS only

Hee-Jung Kang¹, Jung-Moon Yoo^{2,*}, Myeong-Jae Jeong³, and Young-In Won⁴

¹Department of Atmospheric Science and Engineering, Ewha Womans University, Seoul 120-750, Republic of Korea

²Department of Science Education, Ewha Womans University, Seoul 120-750, Republic of Korea

³Department of Atmospheric and Environmental Sciences, Gangneung-Wonju National University, Gangneung 210-702, Republic of Korea

⁴Wyle ST&E, NASA/GSFC, Maryland, USA

13 June 2015 (Revised)

*Corresponding author

Jung-Moon Yoo (yjm@ewha.ac.kr)

Department of Science Education

Ewha Womans University

52, Ewhayodae-gil, Seodaemun-gu, Seoul 120-750, Korea

Office) +82-2-3277-2710, Fax) +82-2-3277-2684

24 Abstract

25 Uncertainties in the satellite-derived Surface Skin Temperature (SST) data in the polar oceans
26 during two periods (April 16-24 and September 15-23) of 2003-2014 were investigated and the three
27 datasets were intercompared as follows: MODerate Resolution Imaging Spectroradiometer Ice
28 Surface Temperature (MODIS IST), the SST of the Atmospheric Infrared Sounder/Advanced
29 Microwave Sounding Unit-A (AIRS/AMSU), and AIRS only. AIRS only algorithm was developed in
30 preparation for the degradation of the AMSU-A. MODIS IST was systematically warmer up to 1.65 K
31 at the sea ice boundary and colder down to -2.04 K in the polar sea ice regions of both the Arctic and
32 Antarctic than that of the AIRS/AMSU. This difference in the results could have been caused by the
33 surface classification method. The spatial correlation coefficient of the AIRS only to the AIRS/AMSU
34 (0.992-0.999) method was greater than that of the MODIS IST to the AIRS/AMSU (0.968-0.994). The
35 SST of the AIRS only compared to that of the AIRS/AMSU had a bias of 0.168 K with a RMSE of
36 0.590 K over the northern hemisphere high latitudes and a bias of -0.109 K with a RMSE of 0.852 K
37 over the southern hemisphere high latitudes. There was a systematic disagreement between the AIRS
38 retrievals at the boundary of the sea ice, because the AIRS only algorithm utilized a less accurate
39 GCM forecast over the seasonally-varying frozen oceans than the microwave data. The three datasets
40 (MODIS, AIRS/AMSU and AIRS only) showed significant warming rates ($2.3\pm 1.7 \sim 2.8\pm 1.9$
41 K/decade) in the northern high regions (70-80 N) as expected from the ice-albedo feedback. The
42 systematic temperature disagreement associated with surface type classification had an impact on the
43 resulting temperature trends.

44

45

46 1. Introduction

47 The satellite observations of the polar oceans have been more **challenging** than those of non-frozen
48 ocean and land, because it is more difficult to identify clouds over the various surfaces (Tobin et al.,
49 2006). The surface skin temperature (SST) is one of the most important climate variables that is
50 related to the surface energy balance and the thermal state of the atmosphere (Jin et al., 1997).
51 Compared to ground-based observations, satellite-observed SST data play a crucial role in climate
52 study and model development by providing a uniform resolution data over the globe. The retrievals of
53 AIRS data over the last decade have a significant contribution to various climate studies and model
54 evaluations (Aumann et al., 2003; Tian et al., 2013; Yoo et al., 2013). AIRS retrievals have produced
55 atmospheric temperature, moisture, and ozone profiles on a global scale by the AIRS method itself or
56 together with other instruments (Liu et al., 2008). A lot of comparisons of the AIRS/AMSU data
57 against data from numerical forecast model analysis fields, radiosondes, lidar, and retrievals from
58 high-altitude aircraft have been used to assess the accuracy of the retrievals (Tobin et al., 2006;
59 Susskind et al., 2014). The AIRS retrieval algorithm has been developed and validated gradually with
60 clear sky and clear/cloudy conditions over a non-frozen ocean and then the non-polar land and polar
61 cases (Tobin et al., 2006).

62 The **AIRS/AMSU** has an advantage of measuring the radiation penetrating through clouds and polar
63 darkness, and has high spectral resolution and coarse spatial resolution (Dong et al., 2006). However,
64 the AIRS only algorithm using only AIRS observations has been developed due to the degradation of
65 the AMSU-A. Microwave and multispectral radiometers were used for global mapping of the sea ice
66 extent and dynamics, while the visible, near-infrared, and infrared sensors could obtain details on the
67 ice concentration, snow/ice albedo, thickness, and IST during clear-sky conditions (Hall et al., 2004;
68 Scott et al., 2014). The MODIS on **Earth Observing System (EOS) Aqua**, used as infrared
69 measurements, was influenced by water and cloud contamination, but had a higher spatial resolution

70 (Dong et al., 2006). In order to remove the cloud effects in the MODIS IST algorithm, MODIS cloud
71 mask products were used (Hall et al., 2004).

72 Since AIRS and MODIS were co-located on Aqua, they have often been used to make a synergistic
73 algorithm and they have been compared to each other frequently (Li et al., 2005; Molnar and Susskind,
74 2005). Molnar and Susskind (2005) validated the accuracy of the AIRS/AMSU cloud products using
75 MODIS cloud analyses, which have a higher spatial resolution than that of AIRS. Knuteson et al.
76 (2006) compared the MODIS Collection 4 (C4) with the AIRS Version 3 (V3) on the land surface
77 temperature (LST) for the eastern half of the U.S., showing that the monthly differences were
78 approximately 3 K. Lee et al. (2013) investigated the characteristics of the differences between the
79 MODIS land surface skin temperature/sea surface temperature and the AIRS/AMSU surface skin
80 temperature across the globe, and found that the MODIS C5 product was systematically lower by 1.7
81 K than the AIRS/AMSU V5 product over land in the 50 N-50 S regions, but it was higher by 0.5 K
82 than the AIRS/AMSU product over ocean. Particularly in the sea ice regions, the MODIS annual
83 averages were larger than the AIRS/AMSU values, due to the differential errors in ice/snow
84 emissivity between the retrieval methods (or channels) for the two data products. The differences
85 between the MODIS and AIRS methods were reduced when the MODIS IST and AIRS/AMSU
86 surface skin temperatures were compared for 9-days. The possible reasons for this include the satellite
87 local crossing time (LCT) difference between them **due to the different swath width** in the high
88 latitude regions, and the emissivity difference between microwave and infrared channels, but more
89 comparison studies are necessary for a longer period to pin down the reasons of such skin temperature
90 discrepancies between MODIS and AIRS/AMSU.

91 The primary purpose of this study was to investigate a relative degree of agreement (or
92 disagreement) among **different SST datasets** using the MODIS IST C5, the SST of the AIRS/AMSU,
93 and AIRS only V6. The second purpose of this paper was to analyze the temperature trend differences

94 affected by the temperature differences among different data products. The datasets used in this study
95 were described in section 2. In section 3, we compared the MODIS and AIRS only data with the
96 AIRS/AMSU values. We also analyzed the temperature trends from the three satellite-based datasets
97 in section 4, and in the conclusion we summarized our study.

98

99 **2. Data and methods**

100 The Aqua satellite carrying the AIRS, AMSU and MODIS instruments was launched on May 4,
101 2002 with the Earth's Radiant Energy System (CERES), Humidity Sounder for Brazil (HSB) and the
102 Advanced Microwave Scanning Radiometer-EOS (AMSR-E). It has far exceeded its designed life
103 span of 6 years and has a chance of operating into the 2020's (<http://aqua.nasa.gov/>). The Aqua
104 satellite orbits the earth every 98.8 minutes with an equatorial crossing time going north (ascending)
105 at 1:30 **p.m.** local time (daytime) and going south (descending) at 1:30 a.m. (nighttime) in a sun-
106 synchronous, near polar orbit with an inclination of 98.2° and an operational altitude of 705 km (Tian
107 et al., 2013).

108 As shown in Table 1, we used the datasets of MODIS IST (e.g., Hall et al., 2006) and SSTs of
109 AIRS/AMSU and AIRS only over the northern hemisphere during April 16-24 and over the southern
110 hemisphere on September 15-23 from 2003 to 2014 in order to avoid the polar night when the visible
111 channels of the MODIS did not operate (Hall et al., 2004). The sea surface temperature observed from
112 infrared channels of satellites indicates the values at the skin of sea water, in contrast with the sea
113 surface temperature measured from buoys, of which values represent the temperature of bulk water
114 near the sea surfaces. The infrared sea SST was measured at depths of approximately $10 \mu\text{m}$ within
115 the oceanic skin layer ($\sim 500 \mu\text{m}$) at the water side of the air-sea interface where the conductive and

116 diffusive heat transfer processes dominated (Emery et al., 2001; Donlon et al., 2002; Liou, 2002).

117 As an imaging spectroradiometer, the MODIS with 36 bands has retrieved various physical
118 parameters such as aerosol optical thickness, land and water surface temperature, leaf area index, and
119 snow cover, etc. (Barnes et al., 1998; Hall and Riggs, 2007). MODIS produced the ‘sea ice by
120 reflectance’ and ‘IST’ in order to identify sea ice (Riggs et al., 1999). The ‘sea ice by reflectance’ was
121 determined by the Normalized Difference Snow Index (NDSI), and the reflectance of Band 1 (0.645
122 μm) and Band 2 (0.858 μm). The NDSI was calculated using Band 4 (0.555 μm) and Band 7 (2.130
123 μm). IST is used as another method for identifying sea ice. The IST derived from the “split-window
124 method” in Eq. (1), where bands 31 and 32 are centered at approximately 11 μm and 12 μm ,
125 respectively. The method was applied in order to identify the ice when the IST was less than 271.5 K.
126 The cutoff temperature between water and ice (271.5 K) may vary depending on the region and
127 season. The IST is calculated as follows:

$$128 \text{ IST} = a + b T_{11} + c (T_{11} - T_{12}) + d [(T_{11} - T_{12})(\sec(\theta) - 1)] \quad (1),$$

129 where T_{11} is the brightness temperature (K) in 11 μm , T_{12} is the brightness temperature (K) in 12 μm ,
130 and θ is the scan angle from nadir. The difference between the T_{11} and the skin temperature from the
131 LOWTRAN can be less than 3 K for a skin temperature between 230 K and 260 K (Key et al., 1997).
132 Since the value of T_{11} itself was a good estimate, coefficients a-d were defined for the following
133 temperature ranges: $T_{11} < 240$ K, $240 \text{ K} \leq T_{11} \leq 260$ K, and $260 \text{ K} < T_{11}$ (Riggs et al., 2006). The IST
134 algorithm was only applied to the polar ocean pixels that were determined to be clear by the MODS
135 cloud mask using visible reflectance (Hall et al., 2004). The surface in the IST algorithm was assumed
136 to be snow (Key et al., 1997). MODIS ISTs were provided as daily polar fields with a 4 km by 4 km

137 resolution.

138 The AIRS spectrometer is a high spectral resolution spectrometer with 2,378 channels in the
139 thermal infrared spectrum and 4 bands in the visible spectrum (Won, 2008). The AIRS and AMSU
140 were coupled in order to play a role as an advanced sounding system under clear and cloudy
141 conditions (Aumann et al., 2003). **The AIRS/AMSU algorithm is independent of the GCM, except for
142 the use of GCM surface pressure to determine the bottom boundary conditions** (Molnar and Susskind,
143 2005). V6 is the most current retrieval algorithm since the launch of AIRS instrument, and detailed
144 descriptions are given in Olsen (2013b). The primary products from AIRS suite include the
145 atmospheric temperature-humidity profiles, ozone profiles, sea/land surface skin temperature (SST),
146 and cloud related parameters such as the outgoing longwave radiation (OLR) (Susskind et al., 2011).
147 In the AIRS/AMSU algorithm, the surface classification was conducted using the brightness
148 temperature difference in 23 GHz (AMSU ch1) and 50 GHz (AMSU ch3). The difference (brightness
149 temperature at 23 GHz minus brightness temperature at 50 GHz) had a negative value on the sea ice
150 and a positive value on the water (Grody et al., 1999; Hewison and English, 1999). Also, the
151 brightness temperature difference between 23 GHz (AMSU ch1) and 31 GHz (AMSU ch2) could
152 distinguish the age of the sea ice (Kongoli et al., 2008). **The accuracy of AIRS/AMSU SST can be
153 affected by surface misclassification, which is caused by the surface emissivity changes, the pixel
154 mixed with the various surface types, and the ice pixel pooled with water.**

155 After the surface type classification from the AMSU retrieval, the initial state for atmospheric
156 and surface parameters, cloud parameters and OLR was generated using the Neural Network
157 methodology (Susskind et al., 2011, 2014). The methodology was used to approximate some functions
158 between the input and output vectors by training (Gardner and Dorling, 1998). Next, the initial clear
159 column radiances were generated, which were based on the initial state and the observed infrared
160 radiances. The surface and atmospheric variables, including the surface skin temperature, were

161 retrieved by updating the cloud cleared infrared radiance, iteratively. The cloud properties and
162 outgoing longwave radiation were then retrieved, followed by the error estimates and quality control.
163 In the AIRS only V6, shortwave window region 3.76–4.0 μm was used in order to derive the surface
164 skin temperature and surface spectral emissivity (ϵ).

165 AMSU channels 4-5 had not been available since 2007 and 2010, respectively, due to radiometric
166 noise. In preparation for the degradation of the other AMSU channels, the AIRS only algorithm was
167 developed excluding the AMSU observations. The algorithm was similar to that of AIRS/AMSU, but
168 it did not use the AMSU-A observations in any step of the physical retrieval process and the quality
169 control methodology. Instead, the AIRS only algorithm used the NOAA Global Forecast System (GFS)
170 for surface classification purposes (Olsen, 2013a).

171 We calculated the climatology and anomaly values from the yearly 9-day mean temperatures in a 1°
172 by 1° grid for the 12-year period of Aqua satellite observations in order to estimate the temperature
173 anomaly trends. The trends of the MODIS IST were derived only when the number of yearly data was
174 at least 10 out of 12 entire years at each grid point. The trends of the AIRS/AMSU and AIRS only
175 were derived only when the number of yearly datasets was 12, covering the entire years of the
176 analysis at each grid. The bootstrap method (Wilks, 1995) was used to calculate at a 95% confidence
177 interval. In the method, 10,000 linear temperature trends were generated by random sampling,
178 allowing repetition of 10,000 yearly anomaly temperature datasets. Then, we estimated the 95%
179 confidence interval of 10,000 temperature trends.

180

181 **3. Comparison of the satellite-derived surface skin temperatures**

182 Figure 1a shows the spatial coverage and the averaged value of the MODIS IST over the southern

183 hemisphere during September 15-23 of 2003-2014. In order to solve the spatial resolution mismatches,
184 the original resolution of the MODIS data with a 4 km by 4 km grid (Fig. 1a) was re-gridded to a 1°
185 by 1° grid in the case of MODIS data present over 50 % (Fig. 1b). A grid spacing of 1° corresponds to
186 approximately 111 km on the equator, and it becomes reduced poleward. In the zonal averaged SST
187 analysis, this 50% criterion was used. During the same period, the spatial distributions of the
188 climatological T_{skin} (AA_V6) and T_{skin} (AO_V6) were also shown in Fig. 1c-d, respectively. As
189 expected, the MODIS and AIRS showed the spatial distribution of the climatological SST, warmer at
190 the lower latitudes than the higher latitudes. The SST distributions over the northern hemisphere
191 during April 16-24 of 2003-2014 have been shown in Kang and Yoo (2015).

192 Figure 2a displays the number of years when both T_{skin} (MODIS) and T_{skin} (AA_V6) are available at
193 each grid point over the southern hemisphere. The number near 60 S was smaller than that of the other
194 regions because the MODIS IST algorithm only produced its data in the cloud-free pixels. Similar
195 distributions by the clouds were shown in Fig. 2b and 2d for the same reason. The reduced number of
196 observations near 60 S had a spatial distribution similar to that of the frontal cloud bands that were
197 likely associated with the mid-/high-latitude depressions encircling the Antarctica (e.g., Jakob, 1999;
198 Comiso and Stock, 2001; Lachlan-Cope, 2010; Boucher et al., 2013). Figure 2c shows the number of
199 years when both T_{skin} (AO_V6) and T_{skin} (AA_V6) were available at each grid. Most of the grids had
200 both T_{skin} (AO_V6) and T_{skin} (AA_V6) for a period of more than 10 years.

201 Figure 3a presents the spatial distribution of the temporal difference in a 1° x 1° grid between the
202 climatological T_{skin} (MODIS) and T_{skin} (AA_V6) during April 16-24 of 2003-2014 over the northern
203 hemisphere. In general, T_{skin} (MODIS) at 60-70 N was higher than the T_{skin} (AA_V6). T_{skin} (MODIS)
204 was about 3 K higher than the T_{skin} (AA_V6) on the Hudson Bay and near Greenland, whereas it was
205 about -2 K lower near the center of the Arctic Ocean. The relationship between the climatological T_{skin}
206 (MODIS) and T_{skin} (AA_V6) was presented in the scatter diagrams (Fig. 3b). The scatter plot revealed

207 a temperature interval which deviated from the simple linear line. The discontinuous shape appeared
208 at the freezing point (~ 273 K) and the turning point (~ 260 K) in terms of T_{skin} (MODIS), changing the
209 coefficient of the MODIS IST algorithm. In the interval, T_{skin} (MODIS) was systematically higher than
210 the T_{skin} (AA_V6) in the 260 – 273 K range of T_{skin} (MODIS). The slope in the range was 0.85, lower
211 than the slope for the whole regression line (0.97). There was a better agreement in the 240-260 K
212 range, where the difference between the T_{11} and the SST in the LOWTRAN was less than 3 K (Key et
213 al., 1997). The better agreement in the range greater than 280K was also shown.

214 Figure 3b was the same as Fig. 3a except for T_{skin} (MODIS) vs. T_{skin} (AO_V6). The differences
215 between the two datasets were very similar to those in Fig. 3a. However, T_{skin} (MODIS) was more
216 than 4 K higher than T_{skin} (AO_V6) in some regions near the Greenland and the Barents Sea. The
217 slope (0.93) in the 260 – 273 K range of T_{skin} (MODIS) also indicated a deviation from the total slope
218 (0.98) in the scatter plot (Fig. 3d), similar to that in Fig. 3b. Figure 3e showed the difference between
219 T_{skin} (AO_V6) to T_{skin} (AA_V6). Overall, the agreement was much better than the previous two cases
220 (Fig. 3a and c), except for in the Greenland Sea, the Barents Sea, and the Okhotsk Sea. Both T_{skin}
221 (AO_V6) and T_{skin} (AA_V6) agreed with each other ($r=0.999$) well except for near the freezing point.

222 Figure 4 showed discrepancies among the three types of SST datasets over the southern hemisphere
223 during September 15-23 of 2003-2014. It has been noted that there was a latitudinal band encircling
224 Antarctica at 60-70 S, where T_{skin} (MODIS) was higher than both the T_{skin} (AA_V6) and T_{skin} (AO_V6)
225 (Fig. 4a and c). The circular region corresponded to the sea ice/water boundary which was expected to
226 move seasonally. This implies a systematic difference between T_{skin} (MODIS) and T_{skin} (AA_V6) in
227 the sea ice classification. The corresponding scatter plots also revealed a discontinuous (i.e., not linear)
228 shape in the 260 – 273 K range of T_{skin} (MODIS) (Fig. 4b and d). The slopes in that range were 0.84-
229 0.94, which were smaller than the slope (0.98) in the whole range. In addition, T_{skin} (MODIS) showed
230 lower temperature values than T_{skin} (AA_V6) and T_{skin} (AO_V6) near the Antarctic peninsula, in the

231 region from Weddell Sea to Ross Sea (Fig. 4a and c).

232 The comparison between two types of AIRS datasets also showed the circular pattern around
233 Antarctica where $T_{\text{skin}}(\text{AO_V6})$ was lower by 1.5-5.6 K than $T_{\text{skin}}(\text{AA_V6})$ (Fig. 4e). The discrepancy
234 near the sea ice/water boundary was clear, possibly due to the difference in the sea ice detection
235 method between the two datasets. The uncertainty of the SST at the sea ice boundary was
236 distinguished from the other regions. Both $T_{\text{skin}}(\text{AO_V6})$ and $T_{\text{skin}}(\text{AA_V6})$ were in good agreement,
237 other than the sea ice/water boundary regions. The scatter pattern of the $T_{\text{skin}}(\text{AA_V6})$ versus that of
238 the $T_{\text{skin}}(\text{AO_V6})$ showed that the two datasets generally agreed with each other, but the disagreement
239 near the freezing point again occurred indicating a cold bias of AIRS only with respect to
240 AIRS/AMSU (Fig. 4f).

241 Figure 5 showed the annual-average spatial distributions for $T_{\text{skin}}(\text{MODIS})$ minus $T_{\text{skin}}(\text{AA_V6})$ in
242 the southern hemisphere from September 15-23 of 2003-2014. Although the 9-day composite values
243 were used in each year, $T_{\text{skin}}(\text{MODIS})$ data did not exist in some areas. It was because the MODIS
244 IST algorithm was valid only for cloud-free pixels. The systematic positive values at the boundary of
245 the sea ice consistently occurred, while the negative ones occurred on some areas of the sea ice near
246 Antarctica every year.

247 Figure 6 presented the interannual variation of the spatial distribution of $T_{\text{skin}}(\text{AO_V6})$ minus T_{skin}
248 (AA_V6) for the study period. As already seen in Fig. 4e, the values of $T_{\text{skin}}(\text{AO_V6})$ compared to
249 $T_{\text{skin}}(\text{AA_V6})$ show systematic negative values encircling Antarctica during the period. In addition,
250 there were positive values over the sea-ice prevailing areas inside the circle, with the location varying
251 from year to year, which must be related to the difference in the surface type characterization.

252 Table 2 showed the statistics of bias, spatial correlation coefficient (r), and root mean square error
253 (RMSE) obtained from the 12-year climatologies of 2003-2014 in order to analyze the systematic

254 error among the three **types** of satellite-observed temperatures quantitatively. This analysis for each
255 hemispheric vernal period has been performed over the two regions (35-90 N, 60-90 N) of the
256 northern hemisphere during April 16-24, and over the regions (40-90 S, 60-90 S) of the southern
257 hemisphere during September 15-23. **The spatial correlation coefficient between the two satellite data**
258 **sets was computed in this study as follows; i) The climatological 9-day composite data of SSTs**
259 **during 2003-2014 were computed in a $1^\circ \times 1^\circ$ grid of the two data sets, respectively. ii) We**
260 **computed the spatial correlation coefficient between the two datasets, using their climatological**
261 **values in a $1^\circ \times 1^\circ$ grid within a given latitude band.** The values in parentheses indicated the average
262 obtained from the statistics for each year and their corresponding standard deviations. Based on the
263 climatology values, the SST of the AIRS retrievals were comparable with respect to the T_{skin} (MODIS)
264 ($r=0.959-0.994$). T_{skin} (MODIS) tended to systematically **exceed** the AIRS retrievals over the polar
265 oceans (bias = 0.198-0.597 K). Hall et al. (2004) reported the accuracy of T_{skin} (MODIS) with the bias
266 values of 1.2-1.3 K near the South Pole and the Arctic Ocean. The RMSE of 1.847 K for T_{skin} (MODIS)
267 vs. the T_{skin} (AA_V6) over 60-90 S in our study was slightly higher than that in the study of Hall et al.
268 (2004).

269 From the intercomparison of the three datasets, the bias (-0.109-0.597) and RMSE (0.590-2.173)
270 over the high latitude belt (60-90 N and S) tended to be larger, and the correlation coefficients
271 ($r=0.959-0.986$) was smaller than those over 35-90 N and 40-90 S among the three comparisons
272 (Table 2). This result indicated that there was more disagreement over the high latitudes than over
273 other regions. The spatial correlation coefficient (0.992-0.999) between T_{skin} (AO_V6) and T_{skin}
274 (AA_V6) was greater than those (0.968-0.994) between T_{skin} (MODIS) and T_{skin} (AA_V6). In the high
275 latitudes T_{skin} (AO_V6) with respect to T_{skin} (AA_V6) had a positive bias of 0.168 K with a RMSE of
276 0.590 K in the northern hemisphere, but a bias of -0.109 K with a RMSE of 0.852 K in the southern
277 hemisphere. The high correlations ($r = 0.998-0.999$) between the AIRS/AMSU and AIRS only (i.e.,

278 AIRS retrievals) over the 35-90 N and 40-90 S areas showed that the AIRS only can be a good
279 alternative for the AIRS/AMSU, except for at the region of the sea ice boundary ($r = 0.992$ over the
280 60-90 S). The disagreement between $T_{\text{skin}}(\text{AA_V6})$ and $T_{\text{skin}}(\text{AO_V6})$ at the region where the sea ice
281 and water mixed appeared, because the AIRS only used less accurate GCM forecast data for surface
282 classification over the potentially frozen oceans.

283 Figure 7 presents the zonal mean temperature difference among the three satellite-observed datasets
284 in a $1^\circ \times 1^\circ$ grid over the northern hemisphere during April 16–24 of 2003-2014 and over the
285 southern hemisphere during September 15-23, 2003-2014. The red, blue and green lines represent the
286 zonally averaged annual values of $T_{\text{skin}}(\text{MODIS})$ minus $T_{\text{skin}}(\text{AA_V6})$, $T_{\text{skin}}(\text{MODIS})$ minus T_{skin}
287 (AO_V6) , and $T_{\text{skin}}(\text{AO_V6})$ minus $T_{\text{skin}}(\text{AA_V6})$, respectively. The climatological annual values
288 have been calculated from the interannually-varying yearly data, shown in Fig. 8. The black dashed
289 line, the difference between the original MODIS IST data (4km x 4km) and converted $T_{\text{skin}}(\text{MODIS})$
290 ($1^\circ \times 1^\circ$) indicated the possible error from the conversion of spatial resolution. The differences by the
291 conversion over both hemispheres were within 0.3 K and 0.5 K, respectively. The original T_{skin}
292 (MODIS), converted $T_{\text{skin}}(\text{MODIS})$, $T_{\text{skin}}(\text{AA_V6})$, and $T_{\text{skin}}(\text{AO_V6})$ were chosen under the same
293 condition in space and time, and each grid ($1^\circ \times 1^\circ$) of a degree latitudinal band.

294 It is hard to see in Fig. 3a the systematic difference due to the sea ice detection over the northern
295 hemisphere because of the continental distribution. However, Fig. 7 clearly showed that the difference
296 among the $T_{\text{skin}}(\text{MODIS})$, $T_{\text{skin}}(\text{AA_V6})$, and $T_{\text{skin}}(\text{AO_V6})$ existed over the northern hemisphere.
297 $T_{\text{skin}}(\text{MODIS})$ was warmer than $T_{\text{skin}}(\text{AA_V6})$ in 56-81 N and 54-69 S, while cooler than $T_{\text{skin}}(\text{AA_V6})$
298 in the other latitudinal zone. It has been noted that the peak of the difference between $T_{\text{skin}}(\text{MODIS})$
299 and two AIRS datasets in the northern hemisphere high-latitude region took place in a broader region
300 than in the southern hemisphere. $T_{\text{skin}}(\text{MODIS})$ was up to 1.65 K higher than the AIRS datasets at the
301 boundaries of the sea ice/water, whereas it was lower by up to -2.04 K over the sea ice region. The

302 MODIS IST algorithm was the optimized on the snow/ice surface type, and thus the underestimation
303 of T_{skin} (MODIS) in the 35-54 N and 40-55 S may not be unexpected. In general, the overestimation of
304 T_{skin} (MODIS) to the AIRS retrievals occurred at the sea ice boundary and the underestimation
305 occurred in the sea ice region that can be covered with snow/ice.

306 The grey solid lines in Fig. A1a-b mean the 5% significance level of the differences between T_{skin}
307 (MODIS) and T_{skin} (AA_V6), and between T_{skin} (AO_V6) and T_{skin} (AA_V6) over a possibly frozen
308 region (poleward from 50 N and 50 S, respectively). Based on the *t*-test (von Storch and Zwiers, 1999)
309 at significance level of $p < 0.05$, the temperature disagreement between T_{skin} (MODIS) and T_{skin}
310 (AA_V6) (red solid line) is significant in 50-55 N, 58-70 N, 89-90 N, 50-53 S, and 57-62 S (Fig. A1a).
311 Considering the uncertainty of MODIS due to the conversion of spatial resolution (black dashed line),
312 the temperature disagreement in 57-62 S can become insignificant. However, the discrepancy in 58-70
313 N is significant even if the uncertainty of MODIS is considered. The difference between T_{skin} (AO_V6)
314 and T_{skin} (AA_V6) in 53-60 S is significant (Fig. A1b).

315 The color-coded lines in Fig. 8 interannually represent the differences in temperature among the
316 three datasets for individual years. The thick black lines indicated the yearly difference averages.
317 There existed a significant degree of interannual variation in the difference between T_{skin} (MODIS)
318 and the two AIRS datasets (Fig. 8a-b). The variation was larger in 2009, 2010 and 2011 over the
319 regions northward of 60 N and southward of 55 S where sea ice existed. Figure 8b shows a value of
320 T_{skin} (MODIS) minus T_{skin} (AO_V6) that was similar to that in Fig. 8a. T_{skin} (MODIS) was lower than
321 T_{skin} (AO_V6) at the ice surface, but higher than T_{skin} (AO_V6) at the boundary of the sea ice. Figure
322 8c showed the interannual variation of T_{skin} (AO_V6) minus T_{skin} (AA_V6). The interannual variation
323 of the difference between the AIRS retrievals was much larger in the high latitude than in the mid-
324 latitudes. The maximum difference of 1.56 K between the AIRS retrievals was found at 87-88 N in
325 2011.

326 There could be several reasons for the observed differences between T_{skin} (MODIS) and T_{skin}
327 (AA_V6). The main one can be attributed to the difference in the channel used for the retrievals of the
328 skin temperature. The AIRS/AMSU V6 only utilized shortwave window channels for the surface skin
329 temperature, while the MODIS IST algorithm used the longwave window regions. The shortwave
330 window could be mixed with the solar radiation during the daytime, but it was suitable for
331 temperature sounding (Chahine, 1975, 1977; Susskind et al., 2014). The advantage of the longwave
332 window was that its range corresponded to the peak of the infrared radiation emitted from the earth
333 (Prakash, 2000). On the other hand, the longwave window radiation could be affected more by clouds.
334 In order to avoid cloud contamination, the MODIS IST algorithm analyzed the pixel when the
335 MODIS cloud mask was reported as clear sky (Hall et al., 2004). The MODIS cloud mask using
336 visible reflectance had a high accuracy during the daytime, but a lower accuracy during the nighttime
337 due to low illumination. As another reason for the temperature difference, Lee et al. (2013) suggested
338 that there were substantial differences in LCT between MODIS and AIRS in the high latitude regions,
339 since the different scan angles of the two instruments resulted in different footprints, which could lead
340 to the observed difference in temperature. However, we suggested that the surface type classification
341 method could be the primary reason for the temperature difference between the MODIS-based and
342 AIRS-based datasets. AIRS/AMSU SST was retrieved after the surface type was classified. On the
343 other hand, the MODIS IST was calculated without the surface type classification step. Then, the
344 MODIS algorithm categorized pixels being ice if IST was less than the cutoff temperature. MODIS
345 IST was calculated on the snow, sea ice, and ocean, assuming the surface was **snow-covered** (sea ice).
346 The IST was utilized as a criterion for identifying the ice/water which might cause significant
347 disagreement between the T_{skin} (MODIS) and T_{skin} (AA_V6) in the range of 260-273 K.

348

349 **4. Comparison of the surface skin temperature trends from the MODIS and AIRS/AMSU**

350 In order to further investigate the effects of the difference among the satellite-observed
351 temperatures from different measurement techniques or algorithms on the temperature anomaly trend,
352 we calculated the trend in some latitude belts, using the three satellite-observed temperature datasets
353 at each grid during April 16-24 of 2003-2014 (in the northern hemisphere) and September 15-23 of
354 2003-2014 in the southern hemisphere. During this period, an unusually extensive surface melting
355 event was observed in 2012 (Nghiem et al., 2012; Hall et al., 2013; Comiso and Hall, 2014).

356 Table 3 shows the temperature anomaly trend with a 95% confidence level on the 10° latitude belt.
357 We arranged the data of MODIS IST, AIRS/AMSU, and AIRS only under the same condition in space
358 and time. The significant warming trend in 70-80 N was estimated in the following order:
359 AIRS/AMSU (2.83 K/decade) > AIRS only (2.71 K/decade) > $T_{\text{skin}}(\text{MODIS})$ (2.30 K/decade). The
360 warming (0.10 to 0.38 K/decade) at 40-50 N and 50-60 S, and the cooling (-0.08 to -1.94 K/decade) at
361 80-90 N, 60-70 N, 50-60 N, 60-70 S and 70-80 S of the three datasets occurred, but the trends were
362 not significant. Comiso and Hall (2014) reported the SST trend using the Goddard Institute for Space
363 Studies (GISS) dataset as 0.60 K/decade and the trend using the Advanced Very High Resolution
364 Radiometer (AVHRR) dataset as 0.69 K/decade in the Arctic (> 64 N) during 1981-2012. Our result in
365 70-80 N, compared with the above studies, seems to indicate an acceleration in the Arctic warming.

366 The warming trend in the northern hemispheric high latitudes had been known to be caused in part
367 by the well-known positive feedback among snow/ice, surface albedo and temperature (Curry et al.,
368 1995; Comiso and Hall, 2014). $T_{\text{skin}}(\text{MODIS})$ had a greater cooling tendency compared to T_{skin}
369 (AA_V6) in the higher latitude regions (70-90 N and 60-80 S) (Table 3). The trend difference between
370 the two temperatures was -0.69 K/decade at 70-80 S. The trend difference of the $T_{\text{skin}}(\text{AA_V6})$ and
371 $T_{\text{skin}}(\text{AO_V6})$ (i.e., AIRS only minus AIRS/AMSU) was the largest (-0.26 K/decade) at 60-70 N. The
372 cooling trend (-0.90 K/decade) of the $T_{\text{skin}}(\text{AO_V6})$ was greater than that (-0.65 K/decade) of T_{skin}
373 (AA_V6) at the latitude band.

374 Figure 9a-b showed the SST anomaly trends from the T_{skin} (MODIS) in a 1° by 1° grid over the
375 northern hemisphere during April 16-24 of 2003-2014 and over the southern hemisphere during
376 September 15-23 of 2003-2014. The T_{skin} (MODIS) trend was calculated on the grid, which had
377 available data that existed for over 10 years. Figure 9c-d and Fig. 9e-f showed the trend data for T_{skin}
378 (AA_V6) and T_{skin} (AO_V6), respectively, which all had 12-year data, individually. The trend
379 distributions in all three of the datasets were similar over the northern hemisphere. Warming trend in
380 the Beaufort Sea, East Siberian Sea and Kara Sea was detected, while cooling was observed in the
381 Hudson Bay and near Greenland. The significant warming trend appeared at 70-80 N as shown in
382 Table 3, and the trend based on the spatial distribution varied depending on the regions (Fig. 9a, c and
383 e). According to Comiso and Hall (2014), a strong warming trend (> 1.5 K/decade) existed near the
384 Kara Sea and Baffin Bay among the entire Arctic, consistent with the noticeable trend revealed near
385 the Kara Sea in our study. Over the southern hemisphere, there were not enough data to derive a trend
386 for T_{skin} (MODIS) mostly due to clouds. The trend analysis over the sea ice regions from T_{skin} (AA_V6)
387 and T_{skin} (AO_V6) showed a strong cooling trend, especially near the Antarctic peninsula between the
388 Weddell and Ross Seas (Fig. 9d and f). The cooling trend was generally dominant over the southern
389 hemisphere. Marshall et al. (2015) suggested that based on the model experiments, the cooling trend
390 around Antarctica as opposed to the warming trend around the Arctic Ocean was the result of the
391 offset between the greenhouse gas and ozone hole responses, emphasizing the larger cooling effects
392 associated with the Antarctic ozone hole.

393 The 12-year mean of the T_{skin} (MODIS) minus T_{skin} (AA_V6) (Fig. 10a and c) and of the trend
394 difference between T_{skin} (MODIS) and T_{skin} (AA_V6) (Fig. 10b and d) were compared in order to
395 reveal the relationship between the temperature difference and the corresponding trend difference over
396 the northern hemisphere during April 16-24 of 2003-2014 and over the southern hemisphere during
397 September 15-23 of 2003-2014. T_{skin} (MODIS) was higher than T_{skin} (AA_V6) over the bays of

398 Hudson and Baffin, and Bering Sea (Fig. 10a). The warming trend of the T_{skin} (MODIS) was also
399 greater than that of the T_{skin} (AA_V6) over the Hudson Bay and near the Kara Sea (Fig. 10b). The data
400 for the trend difference in the southern hemisphere was not sufficient due to the missing data of
401 T_{skin} (MODIS) in the cloudy condition (Fig. 10d).

402 Figure 11 showed over both hemispheres the 12-year mean of the T_{skin} (AO_V6) minus T_{skin}
403 (AA_V6) (Fig. 11a and c) and the corresponding trend difference of the T_{skin} (AO_V6) and T_{skin}
404 (AA_V6) (Fig. 11b and d). The relationship of the temperature difference and trend difference over
405 the southern hemisphere in Fig. 10 was hard to analyze due to the absence of a T_{skin} (MODIS) trend
406 (Fig. 10c-d). However, Fig. 11c-d clearly showed that the temperature difference had a significant
407 impact on the trend difference over the southern hemisphere. The trend of the T_{skin} (AA_V6) and T_{skin}
408 (AO_V6) agreed well except for at the region of the sea ice boundary, implying that the algorithm
409 identifying the sea ice affected the SST trend.

410 **Uncertainties among satellite observations (T_{skin} (MODIS), T_{skin} (AA_V6), and T_{skin} (AO_V6)) in**
411 **the sea ice region of the northern hemisphere are generally similar to those of the southern hemisphere**
412 **in terms of zonal averages. However, the systematic difference between the observations can be more**
413 **clearly seen in the latter region than in the former region due to more oceanic regions in the southern**
414 **hemisphere (Figs. 10-11, and see also Fig. 7).**

415 Table 4 quantitatively showed how the temperature differences among the three types of SST
416 affected each trend difference over the hemispheric regions poleward either from 50 N (shown in the
417 left side of the table) during April 16-24 of 2003-2014 or from 50 S during September 15-23 of 2003-
418 2014. In the upper portion, the average of the temperature difference and the trend difference in the
419 grid corresponding to the temperature difference condition was used, whereas the average values on
420 the grids that had the same signs for the temperature difference and the trend difference were used in

421 the lower portion. Only the cases where grid number was greater than 100 were considered. The
422 warmer temperature led to relatively warming trend, the cooler temperature led to relatively cooling
423 trend. When the $T_{\text{skin}}(\text{MODIS})$ was greater than $T_{\text{skin}}(\text{AA_V6})$ in the regions poleward from 50 S, the
424 trend difference was in the reduced cooling trend (i.e., warmer direction) as -0.96, -0.66, and -0.21
425 K/decade with the conditions of $T_{\text{skin}}(\text{MODIS})$ minus $T_{\text{skin}}(\text{AA_V6})$ rising as more than 1 K, 1.5 K,
426 and 2 K, respectively. The uncertainty of the satellite-derived temperatures had a substantial effect on
427 the uncertainty of the temperature trends. **The data set has been reduced in the lower section of Table**
428 **4. The sample size can affect the estimated impact of ΔT on ΔTrend , but it looks like that the impact**
429 **on the trends in the lower section is almost consistent with that in the upper section despite the**
430 **reduced sample sizes.**

431

432 **5. Conclusions**

433 The satellite-derived L3 products of MODIS IST and two SSTs from AIRS/AMSU and AIRS only
434 were investigated with a comparative analysis during the vernal periods of 2003-2014: April 16-24
435 over the northern hemisphere and September 15-23 over the southern hemisphere. The original
436 MODIS IST data were regridded onto a $1^\circ \times 1^\circ$ grid box for comparison with the AIRS retrievals. The
437 difference between the original MODIS IST and the converted one was within 0.5 K in a latitudinal
438 belt.

439 The differences among the three types of satellite derived SST data were most prominent over the
440 sea ice regions. $T_{\text{skin}}(\text{MODIS})$ and $T_{\text{skin}}(\text{AA_V6})$ were comparable ($r=0.97-0.99$), but there existed
441 systematic disagreement occurred in the $T_{\text{skin}}(\text{MODIS})$ range of 260-273 K. The southern hemispheric
442 high latitude (60 S-90 S) was the primary contributor to the disagreement between them. In
443 comparison with the $T_{\text{skin}}(\text{AA_V6})$ in a latitudinal belt, **the $T_{\text{skin}}(\text{MODIS})$ was higher by up to 1.65 K**

444 than $T_{\text{skin}}(\text{AA_V6})$ on the boundary of the sea ice/water, whereas it was lower by up to -2.04 K in the
445 sea ice region.

446 The spatial correlation coefficients (0.992-0.999) of the $T_{\text{skin}}(\text{AO_V6})$ and $T_{\text{skin}}(\text{AA_V6})$ over both
447 hemispheres were greater than those (0.968-0.994) between $T_{\text{skin}}(\text{MODIS})$ and $T_{\text{skin}}(\text{AA_V6})$. The
448 $T_{\text{skin}}(\text{AO_V6})$ compared to the $T_{\text{skin}}(\text{AA_V6})$ had a bias of 0.168 K with a RMSE of 0.590 K over the
449 northern hemisphere high latitudes and a bias of -0.109 K with a RMSE of 0.852 K over the southern
450 hemispheric high latitudes. There was a systematic disagreement between the $T_{\text{skin}}(\text{AA_V6})$ and T_{skin}
451 (AO_V6) at the sea ice boundary. It is likely due to the fact that the AIRS only algorithm utilized a
452 less accurate GCM forecast than the microwave data over the seasonally-varying frozen oceans.

453 The temperature differences among the three types of datasets showed a high degree of interannual
454 variations over the latitudinal belts where sea ice existed. The significant warming rates ($2.3 \pm 1.7 \sim$
455 2.8 ± 1.9 K/decade) were revealed by all three datasets in the northern hemispheric high-latitude
456 regions (70-80 N) could be interpreted as the ice-albedo feedback. The discrepancies between the
457 trends of the $T_{\text{skin}}(\text{AA_V6})$ and $T_{\text{skin}}(\text{AO_V6})$ occurred at the sea ice boundary. When the T_{skin}
458 (AA_V6) trends were compared to those of the $T_{\text{skin}}(\text{MODIS})$ or $T_{\text{skin}}(\text{AO_V6})$ in a $1^\circ \times 1^\circ$ grid, the
459 warmer temperature difference tended to lead to a relative warming trend, whereas the cooler
460 temperature difference tended to lead to a relative cooling trend.

461 The systematic disagreement between the $T_{\text{skin}}(\text{MODIS})$ and $T_{\text{skin}}(\text{AA_V6})$ could be caused by (1)
462 the channels used for the surface skin temperature, (2) the cloud contamination, (3) the LCT
463 difference between the MODIS and AIRS, and (4) the surface type classification method. Whereas the
464 AIRS/AMSU V6 used only the shortwave window channels for the surface skin temperature, MODIS
465 IST used the longwave window regions. The MODIS IST product utilized the MODIS cloud mask
466 with visible reflectance, which had lower accuracy during the night (Hall et al., 2004). Lee et al.,

467 (2013) reported that the LCTs between the MODIS and AIRS were almost the same from 60 N-60 S,
468 but they were quite different in the high latitude regions. It is likely that the main cause to the
469 observed SST differences near the sea ice boundary was in the way the surface type was classified.
470 The AIRS/AMSU algorithm conjugated the emissivity difference in the low and high frequency
471 microwave bands (23 and 50 GHz) in order to identify sea ice. However, MODIS IST was calculated
472 without the surface type classification.

473 The AIRS/AMSU L2 data offer the surface type (coastline, land, ocean, two types of sea ice, two
474 types of snow, and glacier/snow), and the AIRS/AMSU L3 data offer the number of these various
475 surface types in a grid. The AIRS only L2 also offer the surface type (coastline, land, ocean, two types
476 of sea ice, and snow), and its L3 data offer the number of these various surface types in a grid. Under
477 the condition without ground truth, the direct validation has a limit because the surface classifications
478 of AIRS/AMSU and AIRS only have some difference. Although the AIRS only has utilized the GCM
479 forecast, there is a good agreement in SST between AIRS/AMSU and AIRS only in most regions.
480 However, the disagreement between them over the land regions of the Sahara desert, parts of Spain
481 and in the US with snow cover at night has been reported (Dang et al., 2012).

482 The SST in the polar region is a useful parameter being used to derive the climate change signal,
483 although it has been challenging to measure an accurate SST. Based on our results from detailed
484 comparative investigation, we cautiously suggested that the observed difference and uncertainty
485 among the satellite-derived SSTs were likely caused by the different sea ice detecting methods used in
486 each algorithm. In addition, the methods also affected the temperature trend. In this study, we aimed
487 to help in understanding characteristics of the infrared and microwave measurements for the surface
488 skin temperature, and the method for identifying sea ice. We believe the results of this study can be
489 useful for the interpretation and the modeling of the climate change associated with the temperature
490 trends.

491

492 Acknowledgements

493 This study was supported by the National Research Foundation of Korea (NRF) grant funded by the
494 Korean Government (MSIP) (NO. 2009-0083527) and the Korean Ministry of Environment as the
495 Eco-technopia 21 project (NO. 201200016003).

496 **6. References**

497

498 Aumann, H. H., Chahine, M. T., Gautier, C., Goldberg, M. D., Kalnay, E., McMillin, L. M.,
499 Revercomb, H., Rosenkranz, P. W., Smith, W. L., Staelin, D. H., Strow, L. L., and Susskind, J.:
500 AIRS/AMSU/HSB on the Aqua mission: Design, science objectives, data products, and processing
501 systems, *IEEE Trans. Geosci. Remote Sensing*, 41, 253-264, doi:10.1109/tgrs.2002.808356, 2003.

502 Barnes, W. L., Pagano, T. S., and Salomonson, V. V.: Prelaunch characteristics of the Moderate
503 resolution Imaging Spectroradiometer (MODIS) on EOS-AM1, *IEEE Trans. Geosci. Remote Sensing*,
504 36, 1088-1100, doi:10.1109/36.700993, 1998.

505 Boucher, O., Randall, D., Artaxo, P., Bretherton, C., Feingold, G., Forster, P., Kerminen, V.-M.,
506 Kondo, Y., Liao, H., Lohmann, U., Rasch, P., Satheesh, S. K., Sherwood, S., Stevens, B., and Zhang,
507 X. Y.: Clouds and Aerosols. In: *Climate change 2013: The physical science basis. Contribution of
508 working group I to the fifth assessment report of the intergovernmental panel on climate change*,
509 Cambridge University Press, Cambridge, UK, 2013.

510 Chahine, M. T.: Remote sounding of cloudy atmospheres. I. The single cloud layer, *Journal of the
511 Atmospheric Sciences*, 31, 233-243, doi:10.1175/1520-0469(1974)031<0233:RSOCAI>2.0.CO;2,
512 1974.

513 Chahine, M. T.: Remote sounding of cloudy atmospheres. II. Multiple cloud formations, *Journal of the
514 Atmospheric Sciences*, 34, 744-757, doi:10.1175/1520-0469(1977)034<0744:RSOCAI>2.0.CO;2,
515 1977.

516 Comiso, J. C., and Hall, D. K.: Climate trends in the Arctic as observed from space, *Wiley Interdiscip.
517 Rev.-Clim. Chang.*, 5, 389-409, doi:10.1002/wcc.277, 2014.

518 Comiso, J. C., and Stock, L. V.: Studies of Antarctic cloud cover variability from 1982 through 1999,
519 *Geoscience and Remote Sensing Symposium, 2001. IGARSS '01. IEEE 2001 International*, 1782-
520 1785, 2001.

- 521 Curry, J. A., Schramm, J. L., and Ebert, E. E.: Sea ice-albedo climate feedback mechanism, *J. Clim.*, 8,
522 240-247, doi:10.1175/1520-0442(1995)008<0240:SIACFM>2.0.CO;2, 1995.
- 523 Dang, H. V. T., Lambrigtsen, B., and Manning, E.: AIRS/AMSU/HSB version 6 level 2 performance
524 and test report, available at: http://disc.sci.gsfc.nasa.gov/AIRS/documentation/v6_docs/v6releasedocs-1/V6_L2_Performance_and_Test_Report.pdf, last access: 8 June 2015, 2012.
- 526 Dong, S. F., Gille, S. T., Sprintall, J., and Gentemann, C.: Validation of the Advanced Microwave
527 Scanning Radiometer for the Earth Observing System (AMSR-E) sea surface temperature in the
528 southern ocean, *J. Geophys. Res.-Oceans*, 111, 16, doi:10.1029/2005jc002934, 2006.
- 529 Donlon, C. J., Minnett, P. J., Gentemann, C., Nightingale, T. J., Barton, I. J., Ward, B., and Murray, M.
530 J.: Toward improved validation of satellite sea surface skin temperature measurements for climate
531 research, *J. Clim.*, 15, 353-369, doi:10.1175/1520-0442(2002)015<0353:tivoss>2.0.co;2, 2002.
- 532 Emery, W. J., Castro, S., Wick, G. A., Schluessel, P., and Donlon, C.: Estimating sea surface
533 temperature from infrared satellite and in situ temperature data, *Bull. Amer. Meteorol. Soc.*, 82, 2773-
534 2785, doi:10.1175/1520-0477(2001)082<2773:esstfi>2.3.co;2, 2001.
- 535 Gardner, M. W., and Dorling, S. R.: Artificial neural networks (the multilayer perceptron) - A review
536 of applications in the atmospheric sciences, *Atmos. Environ.*, 32, 2627-2636, doi:10.1016/s1352-
537 2310(97)00447-0, 1998.
- 538 Grody, N., Weng, F., and Ferraro, R.: Application of AMSU for obtaining water vapor, cloud liquid
539 water, precipitation, snow cover and sea ice concentration, in: Technical proceedings of the tenth
540 international atovs study conference, Colorado, USA, 27 January - 2 February 1999, 230-240, 1999.
- 541 Hall, D. K., and Riggs, G. A.: Accuracy assessment of the MODIS snow products, *Hydrol. Process.*,
542 21, 1534-1547, doi:10.1002/hyp.6715, 2007.
- 543 Hall, D. K., Key, J. R., Casey, K. A., Riggs, G. A., and Cavalieri, D. J.: Sea ice surface temperature
544 product from MODIS, *IEEE Trans. Geosci. Remote Sensing*, 42, 1076-1087,
545 doi:10.1109/tgrs.2004.825587, 2004.
- 546 Hall, D. K., Salomonson, V. V., and Riggs, G. A.: MODIS/Aqua Sea Ice Extent and IST Daily L3
547 Global 4km EASE-Grid Day. Version 5. Boulder, Colorado, USA: National Snow and Ice Data Center,
548 2006.
- 549 Hall, D. K., Comiso, J. C., DiGirolamo, N. E., Shuman, C. A., Box, J. E., and Koenig, L. S.:
550 Variability in the surface temperature and melt extent of the Greenland ice sheet from MODIS,
551 *Geophys. Res. Lett.*, 40, 2114-2120, doi:10.1002/grl.50240, 2013.
- 552 Hewison, T. J., and English, S. J.: Airborne retrievals of snow and ice surface emissivity at millimeter
553 wavelengths, *IEEE Trans. Geosci. Remote Sensing*, 37, 1871-1879, doi:10.1109/36.774700, 1999.
- 554 Jakob, C.: Cloud cover in the ECMWF reanalysis, *J. Clim.*, 12, 947-959, doi:10.1175/1520-

555 0442(1999)012<0947:cciter>2.0.co;2, 1999.

556 Jin, M., Dickinson, R. E., and Vogelmann, A. M.: A comparison of CCM2–BATS skin temperature
557 and surface-air temperature with satellite and surface observations, *J. Clim.*, 10, 1505-1524,
558 doi:10.1175/1520-0442(1997)010<1505:ACOCBS>2.0.CO;2, 1997.

559 **Kang, H.-J., and Yoo, J.-M.: Uncertainties of satellite-observed surface skin temperatures due to sea**
560 **ice in the Arctic ocean: MODIS, AIRS/AMSU and AIRS Only, *J. Korean Earth Sci. Soc.*, 36, 139-157,**
561 **doi:10.5467/JKESS.2015.36.2.139, 2015 (in Korean).**

562 Key, J. R., Collins, J. B., Fowler, C., and Stone, R. S.: High-latitude surface temperature estimates
563 from thermal satellite data, *Remote Sens. Environ.*, 61, 302-309, doi:10.1016/S0034-4257(97)89497-
564 7, 1997.

565 Knuteson, R., Cychosz, J., Lee, S. C., Revercomb, H., Tobin, D., and Vinson, K.: Comparison of LST
566 from AIRS and MODIS from the EOS Aqua platform, 10th symposium on Integrated Observing and
567 Assimilation Systems for the Atmosphere, Oceans, and Land Surface (IOASAOLS), the 86th AMS
568 annual meeting, 2006.

569 Kongoli, C., Boukabara, S., Yan, B., Weng, F., and Ferraro, R.: Sea ice concentration retrievals from
570 variationally retrieved microwave surface emissivities, available at:
571 http://microrad2008.cetem.org/public/presentations/20080314_16.50_Kongoli.pdf, last access: 4
572 December 2014, 2008.

573 Lachlan-Cope, T.: Antarctic clouds, *Polar Res.*, 29, 150-158, doi:10.1111/j.1751-8369.2010.00148.x,
574 2010.

575 Lee, Y.-R., Yoo, J.-M., Jeong, M.-J., Won, Y.-I., Hearty, T., and Shin, D.-B.: Comparison between
576 MODIS and AIRS/AMSU satellite-derived surface skin temperatures, *Atmos. Meas. Tech.*, 6, 445-455,
577 doi:10.5194/amt-6-445-2013, 2013.

578 Li, G., Huang, H.-L., Baggett, K., and Li, J.: Comparison of global AIRS/AMSU and AIRS/MODIS
579 cloud-clearing performance, in: *Proc. SPIE 5890, Atmospheric and Environmental Remote Sensing*
580 *Data Processing and Utilization: Numerical Atmospheric Prediction and Environmental Monitoring*,
581 California, USA, 58901D, 2005.

582 Liou, K. N.: *An introduction to atmospheric radiation*, Academic Press, Amsterdam; Boston;, 2002.

583 Liu, C. Y., Li, J., Weisz, E., Schmit, T. J., Ackerman, S. A., and Huang, H. L.: Synergistic use of AIRS
584 and MODIS radiance measurements for atmospheric profiling, *Geophys. Res. Lett.*, 35, 6,
585 doi:10.1029/2008gl035859, 2008.

586 Marshall, J., Armour, K. C., Scott, J. R., Kostov, Y., Hausmann, U., Ferreira, D., Shepherd, T. G., and
587 Bitz, C. M.: The ocean's role in polar climate change: asymmetric Arctic and Antarctic responses to
588 greenhouse gas and ozone forcing, *Phil. Trans. R. Soc.*, 372, 20130040, doi: 10.1098/rsta.2013.0040,
589 2014.

590 Molnar, G. I., and Susskind, J.: Validation of AIRS/AMSU cloud retrievals using MODIS cloud
591 analyses, in: Proc. SPIE 5806, Algorithms and Technologies for Multispectral, Hyperspectral, and
592 Ultraspectral Imagery XI, 13 July 2005, 618-629, 2005.

593 Nghiem, S. V., Hall, D. K., Mote, T. L., Tedesco, M., Albert, M. R., Keegan, K., Shuman, C. A.,
594 DiGirolamo, N. E., and Neumann, G.: The extreme melt across the Greenland ice sheet in 2012,
595 *Geophys. Res. Lett.*, 39, 6, doi:10.1029/2012gl053611, 2012.

596 Olsen, E.: AIRS/AMSU/HSB version 6 changes from version 5, available at:
597 [http://disc.sci.gsfc.nasa.gov/AIRS/documentation/v6_docs/v6releasedocs-](http://disc.sci.gsfc.nasa.gov/AIRS/documentation/v6_docs/v6releasedocs-1/V6_Changes_from_V5.pdf)
598 [1/V6_Changes_from_V5.pdf](http://disc.sci.gsfc.nasa.gov/AIRS/documentation/v6_docs/v6releasedocs-1/V6_Changes_from_V5.pdf), last access: 4 December 2014, 2013a.

599 Olsen, E.: AIRS/AMSU/HSB version 6 retrieval flow, available at:
600 http://disc.sci.gsfc.nasa.gov/AIRS/documentation/v6_docs/v6releasedocs-1/V6_Retrieval_Flow.pdf,
601 last access: 4 December 2014, 2013b.

602 Prakash, A.: Thermal remote sensing: concepts, issues and application, XIXth ISPRS Congress,
603 Amsterdam, Netherlands, 239-243, 2000.

604 Riggs, G. A., Hall, D. K., and Ackerman, S. A.: Sea ice extent and classification mapping with the
605 Moderate resolution Imaging Spectroradiometer airborne simulator, *Remote Sens. Environ.*, 68, 152-
606 163, doi:10.1016/s0034-4257(98)00107-2, 1999.

607 Riggs, G. A., Hall, D. K., and Salomonson, V. V.: MODIS sea ice products user guide to collection 5,
608 available at: http://modis-snow-ice.gsfc.nasa.gov/uploads/siug_c5.pdf, last access: 7 February 2015,
609 2006.

610 Scott, K. A., Li, E., and Wong, A.: Sea ice surface temperature estimation using MODIS and AMSR-E
611 data within a guided variational model along the Labrador Coast, *IEEE J. Sel. Top. Appl. Earth*
612 *Observ. Remote Sens.*, 7, 3685-3694, doi:10.1109/jstars.2013.2292795, 2014.

613 Susskind, J., Blaisdell, J. M., Iredell, L., and Keita, F.: Improved temperature sounding and quality
614 control methodology using AIRS/AMSU Data: The AIRS science team version 5 retrieval algorithm,
615 *IEEE Trans. Geosci. Remote Sensing*, 49, 883-907, doi:10.1109/tgrs.2010.2070508, 2011.

616 Susskind, J., Blaisdell, J. M., and Iredell, L.: Improved methodology for surface and atmospheric
617 soundings, error estimates, and quality control procedures: the atmospheric infrared sounder science
618 team version-6 retrieval algorithm, *APPRES*, 8, 084994, doi:10.1117/1.JRS.8.084994, 2014.

619 Tian, B. J., Fetzer, E. J., Kahn, B. H., Teixeira, J., Manning, E., and Hearty, T.: Evaluating CMIP5
620 models using AIRS tropospheric air temperature and specific humidity climatology, *J. Geophys. Res.-*
621 *Atmos.*, 118, 114-134, doi:10.1029/2012jd018607, 2013.

622 Tobin, D. C., Revercomb, H. E., Knuteson, R. O., Lesht, B. M., Strow, L. L., Hannon, S. E., Feltz, W.
623 F., Moy, L. A., Fetzer, E. J., and Cress, T. S.: Atmospheric radiation measurement site atmospheric
624 state best estimates for atmospheric infrared sounder temperature and water vapor retrieval validation,

- 625 J. Geophys. Res.-Atmos., 111, 18, doi:10.1029/2005jd006103, 2006.
- 626 von Storch, H. and Zwiers, F. W.: Statistical Analysis in Climate Research, Cambridge University
627 Press, Cambridge, UK, 1999.
- 628 Wilks, D. S.: Statistical methods in the atmospheric sciences, Academic Press, San Diego:, 1995.
- 629 Won, Y.-I.: Readme document for AIRS Level-3 version 5 standard products: daily (AIRH3STD,
630 AIRX3STD, AIRS3STD), 8-day (AIRH3ST8, AIRX3ST8, AIRS3ST8) & monthly (AIRH3STM,
631 AIRX3STM, AIRS3STM), available at:
632 <http://disc.sci.gsfc.nasa.gov/TRMM/AIRS/documentation/readmes/README.AIR-3ST.pdf>, last
633 access: 4 December 2014, 2008.
- 634 Yoo, J.-M., Won, Y.-I., Jeong, M.-J., Kim, K.-M., Shin, D.-B., Lee, Y.-R., and Cho, Y.-J.: Intensity of
635 climate variability derived from the satellite and MERRA reanalysis temperatures: AO, ENSO, and
636 QBO, J. Atmos. Sol.-Terr. Phys., 95-96, 15-27, doi:10.1016/j.jastp.2013.01.002, 2013.

637 Table 1. The information on the satellite-observed surface skin temperature (T_{skin}) Level 3 (L3) data used in this study. Three datasets of T_{skin} were compared
 638 over the northern hemisphere during April 16-24 of 2003-2014, and over the southern hemisphere during September 15-23 of 2003-2014. The abbreviations
 639 used in this table are as follows: temp (temperature), IST (ice surface skin temperature), OBS (observation), and SFC (surface).

Satellite-observed dataset	Version (Collection)	Temp type	Area	Spatial resolution	Number of OBS	Satellite sensor	Abbreviation	Reference
MODIS IST	MYD29E1D/5	Skin	Polar ocean	4km×4km	1/day	Aqua MODIS	$T_{\text{skin}}(\text{MODIS})$	Hall et al.(2004)
AIRS/AMSU SFC skin temp	AIRX3STD/6	Skin	Globe	1°×1°	2/day	Aqua AIRS/AMSU-A	$T_{\text{skin}}(\text{AA_V6})$	Susskind et al. (2014)
AIRS only SFC skin temp	AIRS3STD/6	Skin	Globe	1°×1°	2/day	Aqua AIRS	$T_{\text{skin}}(\text{AO_V6})$	Susskind et al. (2014)

640
 641
 642
 643
 644
 645
 646
 647
 648
 649
 650

651 Table 2. Statistical comparisons of the climatological 9-day composite data during 2003-2014 over both hemispheres; $T_{\text{skin}}(\text{MODIS})$ vs. $T_{\text{skin}}(\text{AA_V6})$, $T_{\text{skin}}(\text{MODIS})$ vs.
652 $T_{\text{skin}}(\text{AO_V6})$, and $T_{\text{skin}}(\text{AO_V6})$ vs. $T_{\text{skin}}(\text{AA_V6})$. The values in this table were calculated based on the 12-year composite mean values. The values in parentheses indicate
653 the 12-year mean values and their standard deviations during 2003-2014. Bias: $T_{\text{skin}}(\text{MODIS})$ minus $T_{\text{skin}}(\text{AA_V6})$, $T_{\text{skin}}(\text{MODIS})$ minus $T_{\text{skin}}(\text{AO_V6})$, and $T_{\text{skin}}(\text{AO_V6})$
654 minus $T_{\text{skin}}(\text{AA_V6})$, r: correlation coefficient, RMSE: root mean square error.

Region	$T_{\text{skin}}(\text{MODIS})$ vs. $T_{\text{skin}}(\text{AA_V6})$			$T_{\text{skin}}(\text{MODIS})$ vs. $T_{\text{skin}}(\text{AO_V6})$			$T_{\text{skin}}(\text{AO_V6})$ vs. $T_{\text{skin}}(\text{AA_V6})$		
	Bias (K)	r	RMSE (K)	Bias (K)	r	RMSE (K)	Bias (K)	R	RMSE (K)
35-90N	-0.169 (-0.161±0.231)	0.994 (0.990±0.002)	1.491 (1.909±0.156)	-0.289 (-0.324±0.308)	0.993 (0.990±0.003)	1.563 (1.963±0.260)	0.133 (0.137±0.130)	0.999 (0.997±0.001)	0.574 (1.018±0.131)
40-90S	0.026 (-0.010±0.218)	0.989 (0.982±0.003)	1.480 (2.082±0.144)	0.203 (0.035±0.282)	0.985 (0.980±0.003)	1.756 (2.184±0.119)	-0.141 (-0.139±0.079)	0.998 (0.994±0.001)	0.750 (1.272±0.092)
60-90N	0.223 (0.194±0.357)	0.986 (0.973±0.009)	1.501 (1.986±0.227)	0.597 (-0.013±0.475)	0.986 (0.972±0.011)	1.591 (2.033±0.370)	0.168 (0.170±0.214)	0.998 (0.992±0.003)	0.590 (1.027±0.216)
60-90S	0.198 (0.368±0.537)	0.968 (0.906±0.023)	1.847 (2.871±0.276)	0.306 (0.295±0.620)	0.959 (0.898±0.021)	2.173 (2.987±0.271)	-0.109 (-0.108±0.142)	0.992 (0.976±0.005)	0.852 (1.498±0.112)

655

656

657

658

659

660 Table 3. The rate of the surface skin temperature change (K/decade) of the MODIS, AIRS/AMSU, and AIRS only in each 10° latitudinal belt over the northern hemisphere
 661 (NH) during April 16-24 and over the southern hemisphere (SH) during September 15-23 of 2003-2014, using their collocated data in a 1°×1° grid. The ± values define the 95%
 662 confidence intervals for the trends. The symbol ‘*’ means the significant value at a 95% confidence interval. Note that the rates are subject to large uncertainty due to the
 663 short periods of the satellite-based temperature records.

Latitudinal belt	MODIS	AIRS/AMSU	AIRS only	MODIS minus AIRS/AMSU	MODIS minus AIRS only	AIRS only minus AIRS/AMSU
<NH>						
80-90 N	-0.558±3.101	-0.100±3.673	-0.093±3.736	-0.458	-0.465	0.007
70-80 N	2.302±1.701*	2.826±1.878*	2.711±1.788*	-0.524	-0.409	-0.115
60-70 N	-0.506±1.173	-0.646±1.294	-0.902±1.050	0.140	0.396	-0.256
50-60 N	-0.345±0.539	-0.522±0.628	-0.466±0.550	0.177	0.121	0.056
40-50 N	0.292±0.402	0.103±0.576	0.191±0.565	0.189	0.101	0.088
<SH>						
50-60 S	0.375±0.400	0.315±0.466	0.316±0.600	0.060	0.059	0.001
60-70 S	-1.944±2.271	-1.304±1.890	-1.300±1.918	-0.640	-0.644	0.004
70-80 S	-0.769±2.687	-0.081±2.586	-0.135±2.633	-0.688	-0.634	-0.054

664
 665
 666
 667
 668
 669
 670
 671
 672
 673
 674

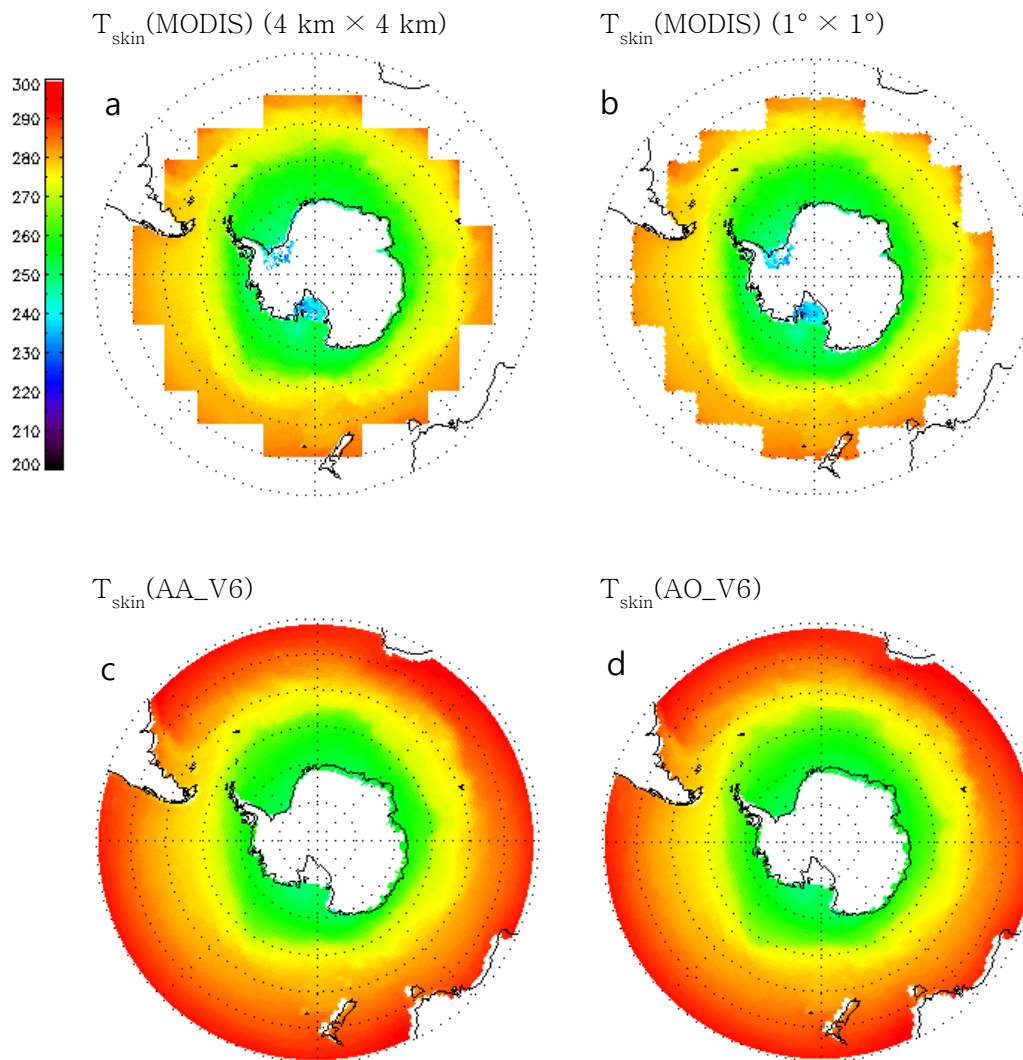
675 Table 4. Uncertainties of the satellite-derived surface skin temperature rate (or trend; ΔTrend) due to the temperature difference (ΔT_{skin}) for the cases of T_{skin} (MODIS) minus
676 T_{skin} (AA_V6) and T_{skin} (AO_V6) minus T_{skin} (AA_V6) in the upper portion of the table. Also, the values of uncertainties provided in the lower portion of the table indicate the
677 cases of $\pm\Delta\text{Trend}$ with respect to $\pm\Delta T_{\text{skin}}$ (double signs in the same order). The uncertainties are not shown when the number of the grid ($1^\circ \times 1^\circ$) points (i.e., No. of grids in
678 the table) is less than 100.
679

ΔT_{skin} (K)	Poleward from 50N						Poleward from 50S					
	T_{skin} (MODIS) vs. T_{skin} (AA_V6)			T_{skin} (AO_V6) vs. T_{skin} (AA_V6)			T_{skin} (MODIS) vs. T_{skin} (AA_V6)			T_{skin} (AO_V6) vs. T_{skin} (AA_V6)		
	No. of grids	ΔT_{skin}	ΔTrend (K/decade)	No. of grids	ΔT_{skin}	ΔTrend (K/decade)	No. of grids	ΔT_{skin}	ΔTrend (K/decade)	No. of grids	ΔT_{skin}	ΔTrend (K/decade)
≥ 1.0	2155	2.01	-0.10	95	-	-	425	2.01	-0.96	378	1.37	0.03
≥ 1.5	1506	2.34	0.04	19	-	-	253	2.25	-0.66	104	1.80	0.24
≥ 2.0	940	2.71	0.19	5	-	-	134	2.69	-0.21	22	-	-
≤ -1.0	1839	-1.59	-0.45	236	-2.25	-0.34	224	-1.71	-0.43	877	-2.19	-0.37
≤ -1.5	921	-1.94	-0.45	162	-2.72	-0.47	115	-2.18	-0.16	654	-2.52	-0.55
≤ -2.0	367	-2.27	-0.60	109	-3.20	-0.78	55	-	-	472	-2.82	-0.69
≥ 1.0	912	2.15	1.21	40	-	-	139	2.09	1.36	179	1.40	1.01
≥ 1.5	707	2.41	1.22	8	-	-	94	-	-	51	-	-
≥ 2.0	499	2.70	1.22	1	-	-	64	-	-	15	-	-
≤ -1.0	1309	-1.59	-0.90	126	-2.51	-2.02	122	-1.69	-2.42	500	-2.26	-1.96
≤ -1.5	643	-1.96	-0.92	89	-	-	61	-	-	387	-2.55	-2.06
≤ -2.0	272	-2.28	-1.02	69	-	-	27	-	-	293	-2.81	-2.06

680

681

Sep 15-23, 2003-2014



682

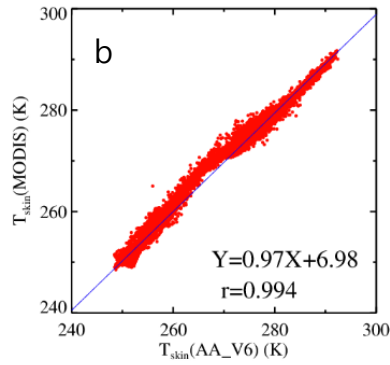
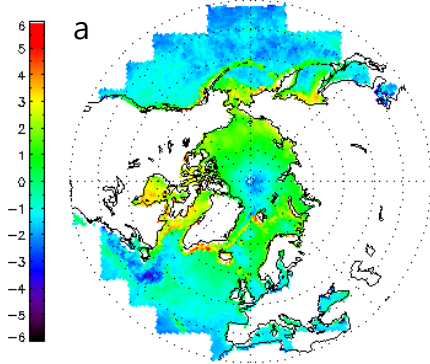
683 Fig. 1. (a) 12-year composite skin temperatures (K) of the MODIS IST over the southern hemisphere during
684 September 15-23 of 2003-2014. The original MODIS data (MYD29E1D) have a $4 \text{ km} \times 4 \text{ km}$ spatial resolution.
685 Their spatial resolution has been reconstructed to $1^\circ \times 1^\circ$ in Fig. 1b in order to compare this data with the
686 AIRS/AMSU data. Figure 1c-d is the surface skin temperatures of the AIRS/AMSU and AIRS only over the
687 southern hemisphere ocean during September 15-23 of 2003-2014, respectively.

688

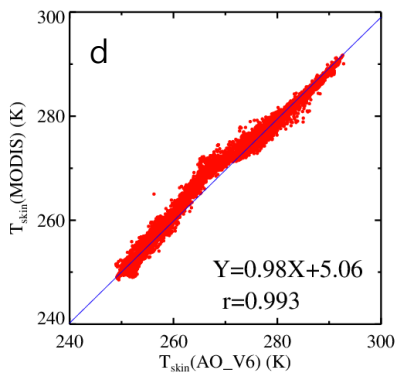
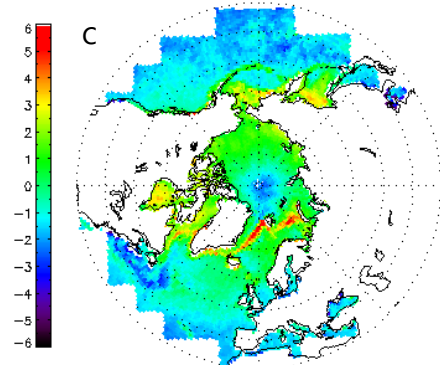
689

690

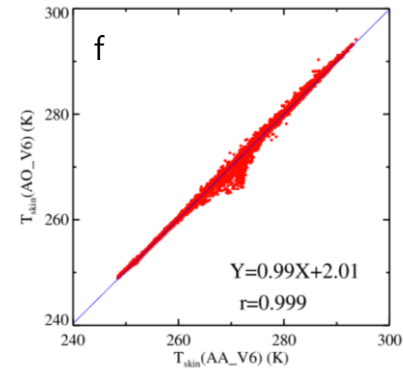
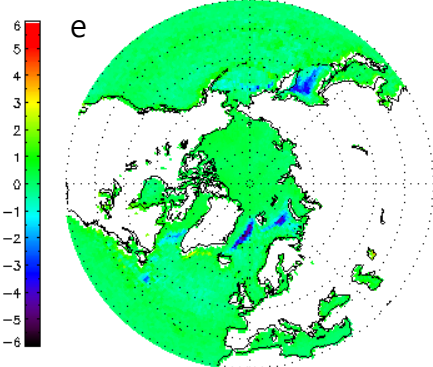
$T_{\text{skin}}(\text{MODIS})$ minus $T_{\text{skin}}(\text{AA_V6})$



$T_{\text{skin}}(\text{MODIS})$ minus $T_{\text{skin}}(\text{AO_V6})$



$T_{\text{skin}}(\text{AO_V6})$ minus $T_{\text{skin}}(\text{AA_V6})$

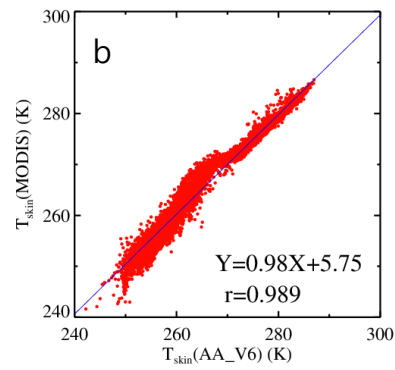
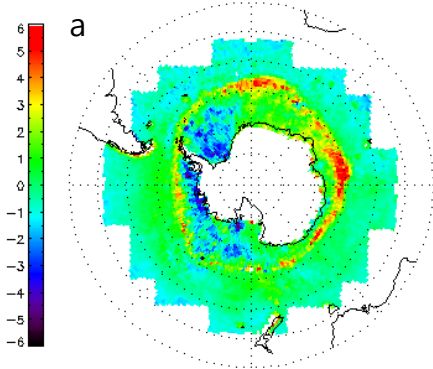


702

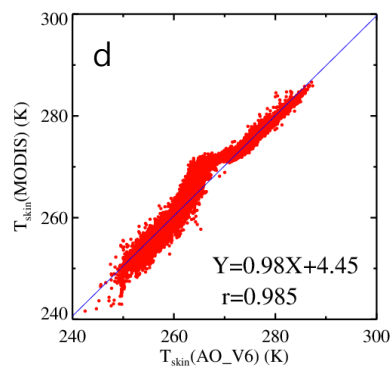
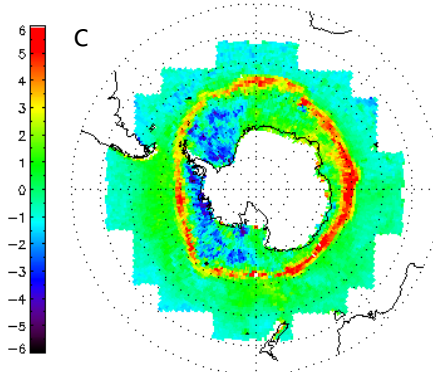
703 Fig. 3. The distributions of (a) $T_{\text{skin}}(\text{MODIS})$ minus $T_{\text{skin}}(\text{AA_V6})$, (c) $T_{\text{skin}}(\text{MODIS})$ minus T_{skin}
704 (AO_V6), and (e) $T_{\text{skin}}(\text{AO_V6})$ minus $T_{\text{skin}}(\text{AA_V6})$ over the northern hemisphere during April 16-
705 24 of 2003-2014. The scatter plots of (b) $T_{\text{skin}}(\text{MODIS})$ versus $T_{\text{skin}}(\text{AA_V6})$, (d) $T_{\text{skin}}(\text{MODIS})$
706 versus $T_{\text{skin}}(\text{AO_V6})$, and (f) $T_{\text{skin}}(\text{AO_V6})$ versus $T_{\text{skin}}(\text{AA_V6})$.

707

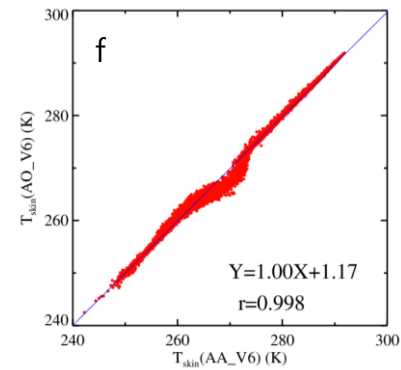
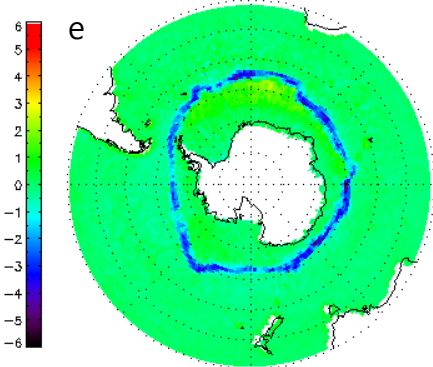
$T_{\text{skin}}(\text{MODIS})$ minus $T_{\text{skin}}(\text{AA_V6})$



$T_{\text{skin}}(\text{MODIS})$ minus $T_{\text{skin}}(\text{AO_V6})$



$T_{\text{skin}}(\text{AO_V6})$ minus $T_{\text{skin}}(\text{AA_V6})$

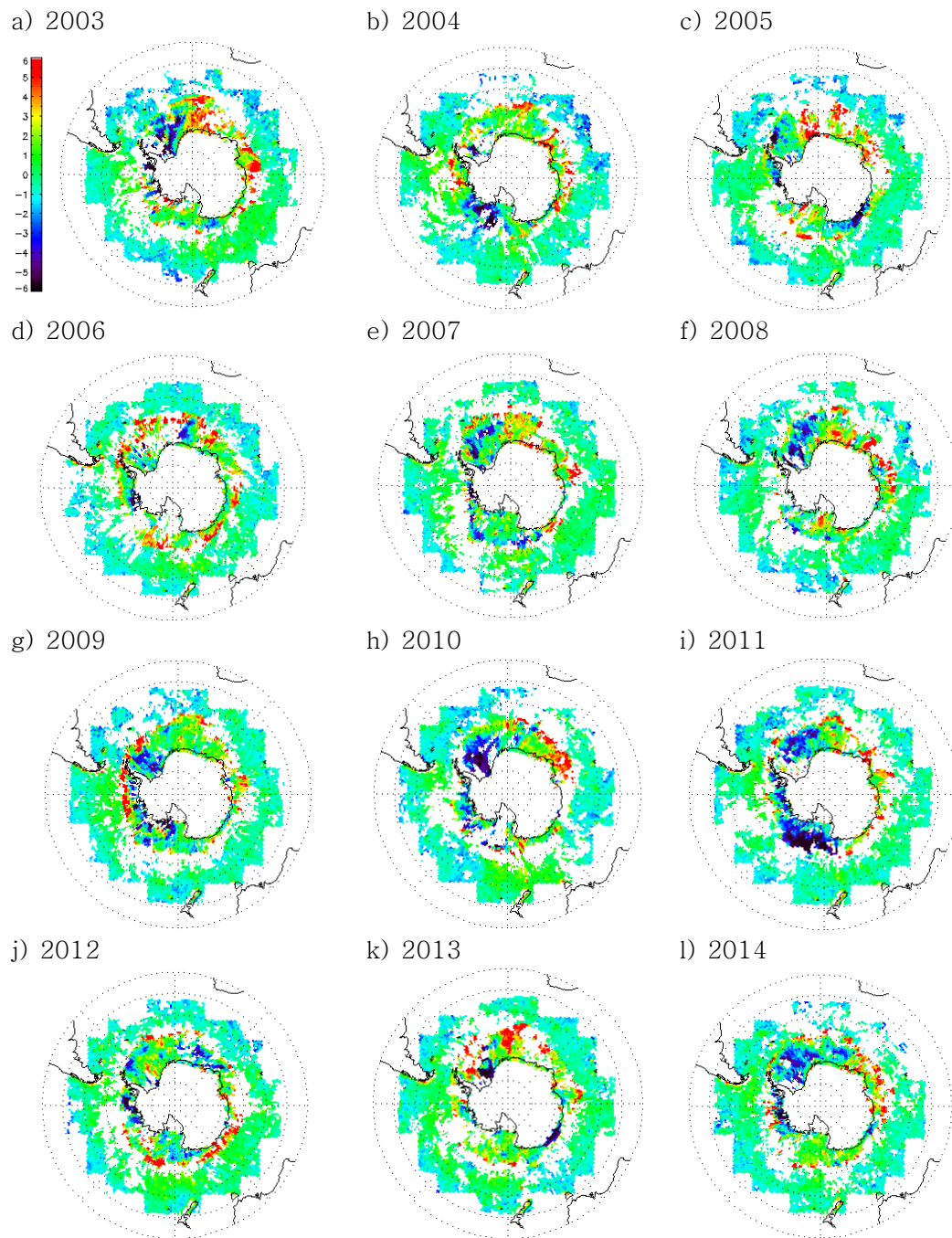


708

709 Fig. 4. Same as in Fig. 3 except for the data taken during September 15-23 of 2003-2014, over the
710 southern hemisphere.

711

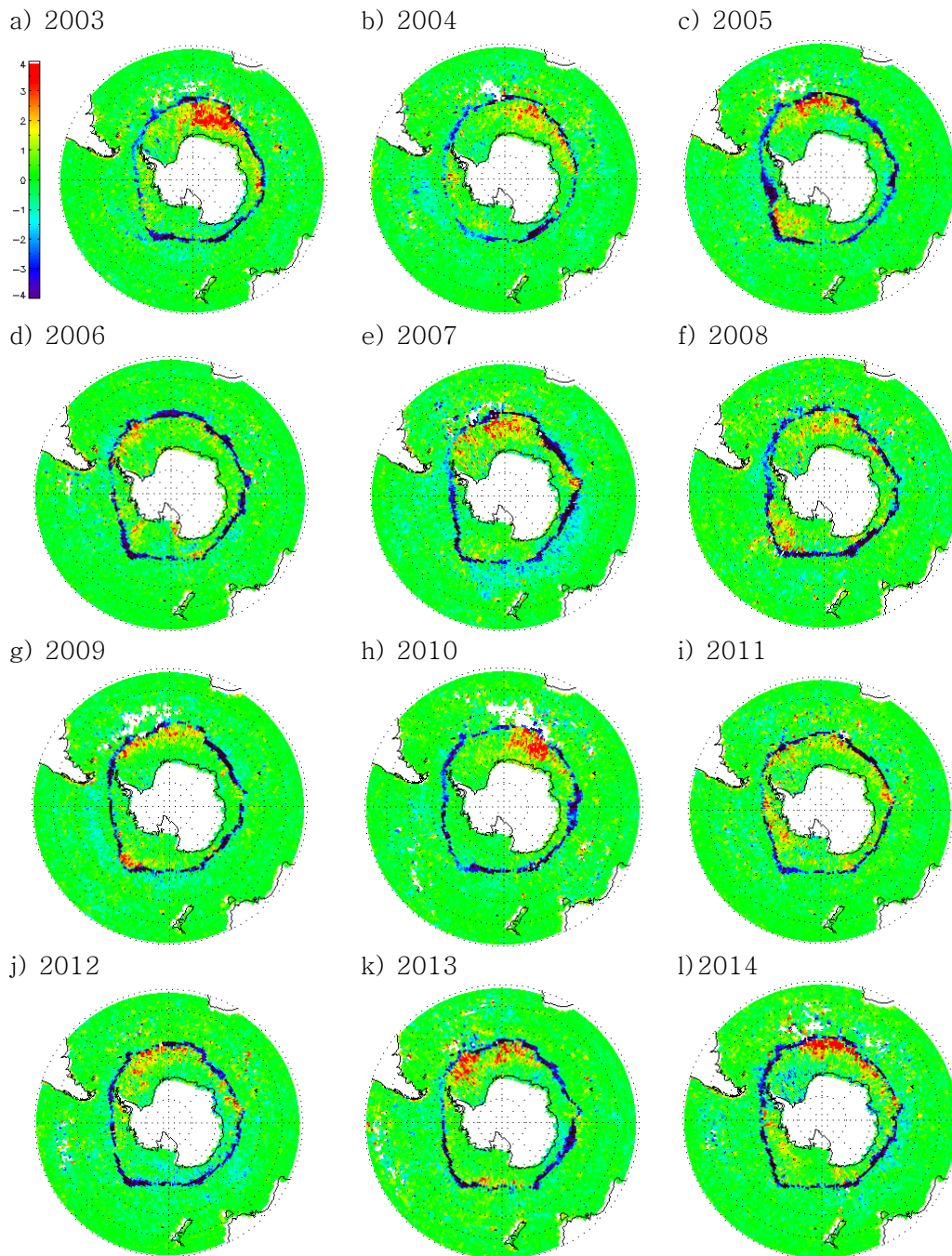
712



714

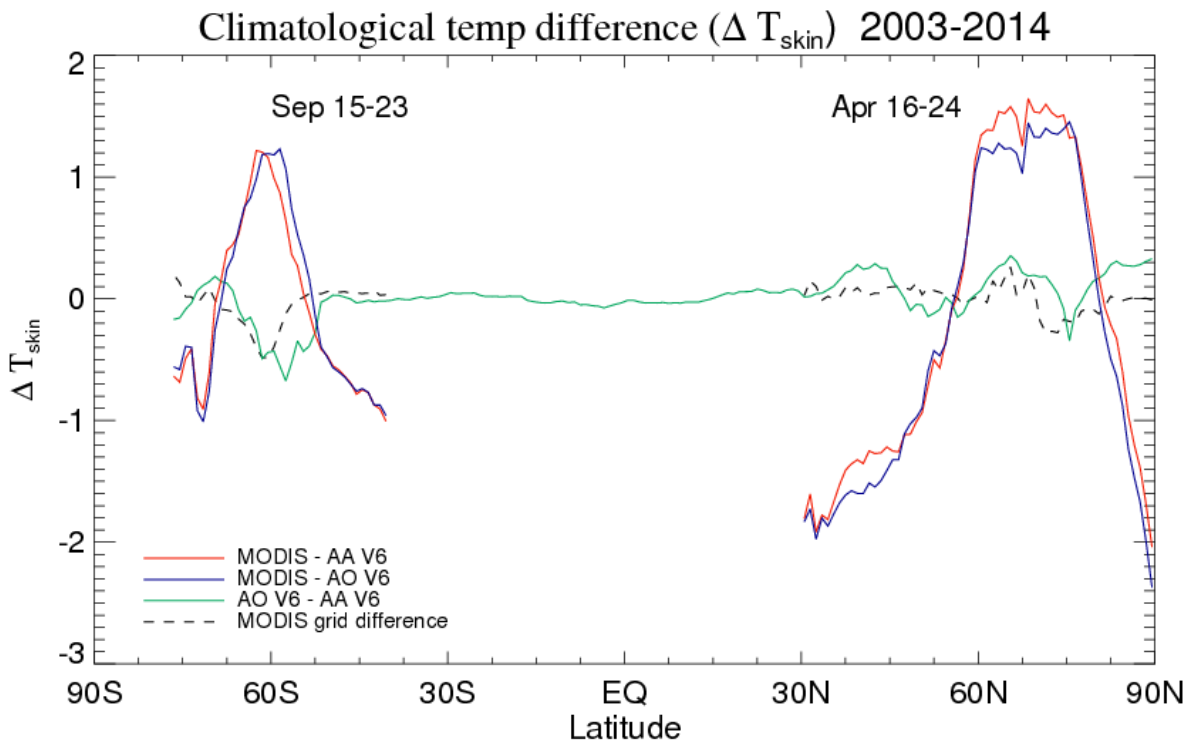
715 Fig. 5. Annual-average spatial distributions of the T_{skin} (MODIS) minus T_{skin} (AA_V6) over the
716 southern hemisphere during September 15-23.

717



720 Fig. 6. Same as Fig. 5 except for $T_{\text{skin}}(\text{AO_V6})$ minus $T_{\text{skin}}(\text{AA_V6})$.

722



723

724 Fig. 7. Zonal averaged values of $T_{skin}(\text{MODIS})$ minus $T_{skin}(\text{AA_V6})$ (red solid line), $T_{skin}(\text{MODIS})$ minus T_{skin}
725 (AO_V6) (blue solid line), and $T_{skin}(\text{AO_V6})$ minus $T_{skin}(\text{AA_V6})$ (green solid line). The difference in spatial
726 grid averages of the MODIS data between 4 km by 4 km and 1° by 1° is shown by the black dashed line. The
727 difference values are calculated at one degree interval along each latitudinal belt. The climatological data
728 periods are April 16-24, 2003-2014 over the northern hemisphere, and September 15-23, 2003-2014 over the
729 southern hemisphere.

730

731

732

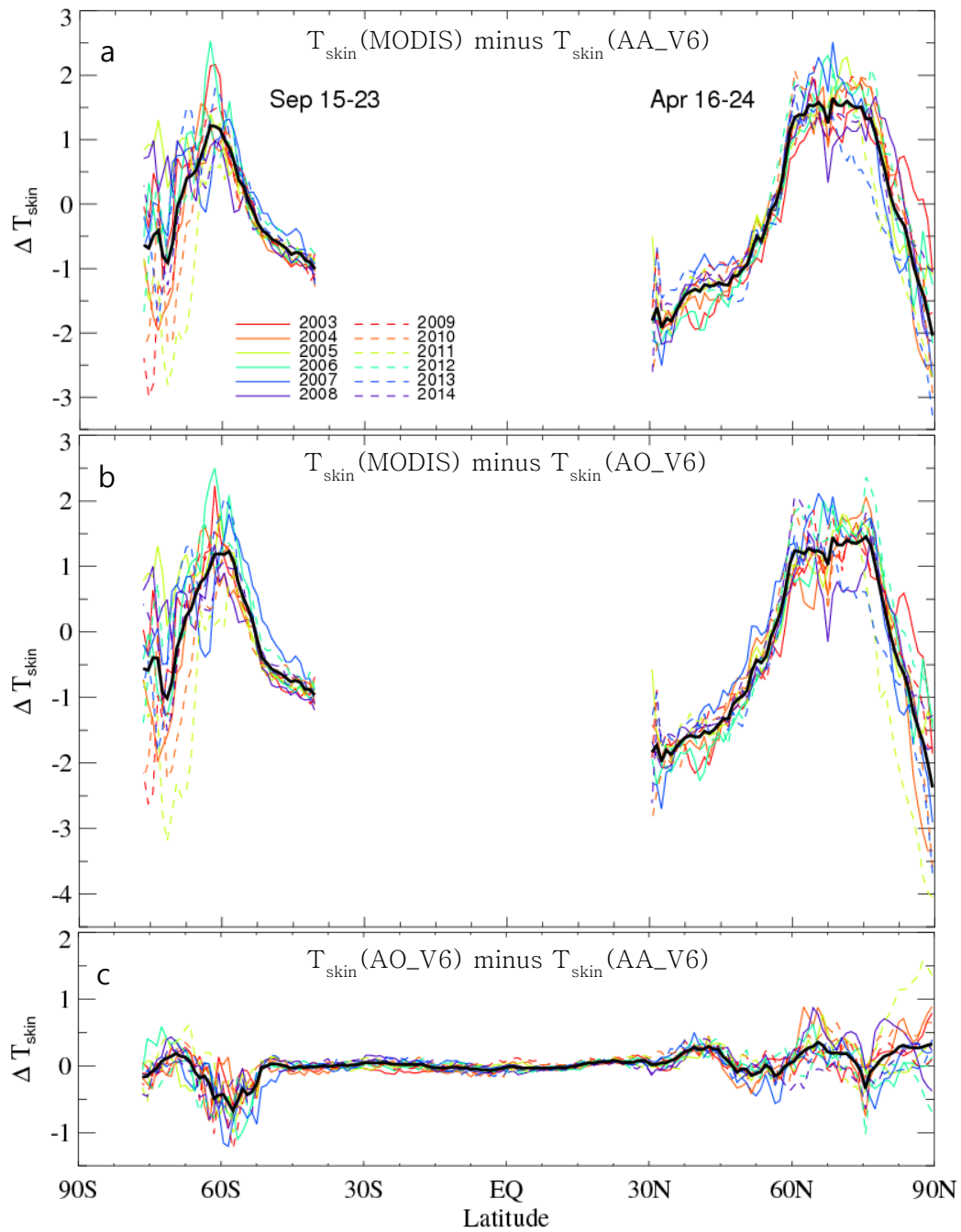
733

734

735

736

737



738

739

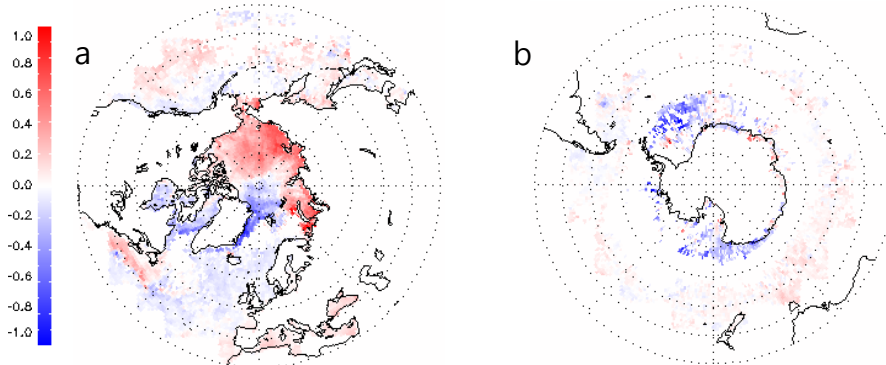
740 Fig. 8. Zonal averaged values of (a) $T_{skin}(MODIS) \text{ minus } T_{skin}(AA_V6)$, (b) $T_{skin}(MODIS) \text{ minus } T_{skin}(AO_V6)$, (c) T_{skin}
 741 $(AO_V6) \text{ minus } T_{skin}(AA_V6)$ over the northern hemisphere from April 16 to 24, 2003-2014, and over the southern
 742 hemisphere from September 15 to 23, 2003-2014. The values in each year represent the corresponding color lines. The thick
 743 black line indicates the mean difference values.

Apr 16-24

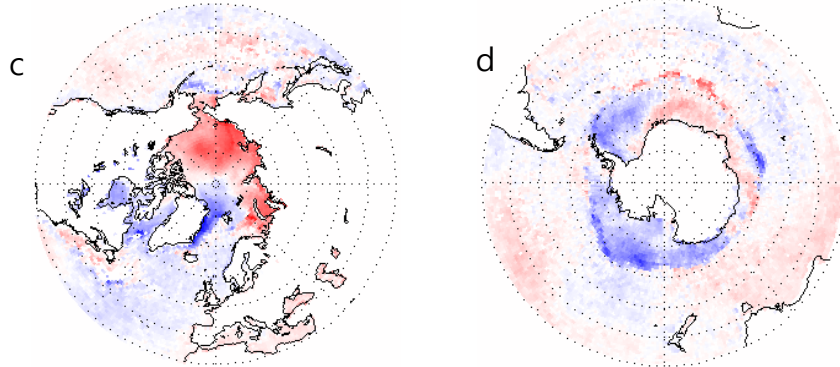
2003-2014

Sep 15-23

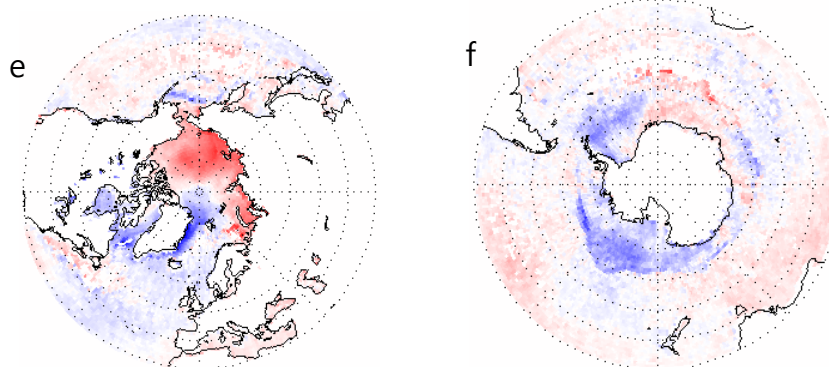
$T_{\text{skin}}(\text{MODIS})$



$T_{\text{skin}}(\text{AA_V6})$



$T_{\text{skin}}(\text{AO_V6})$



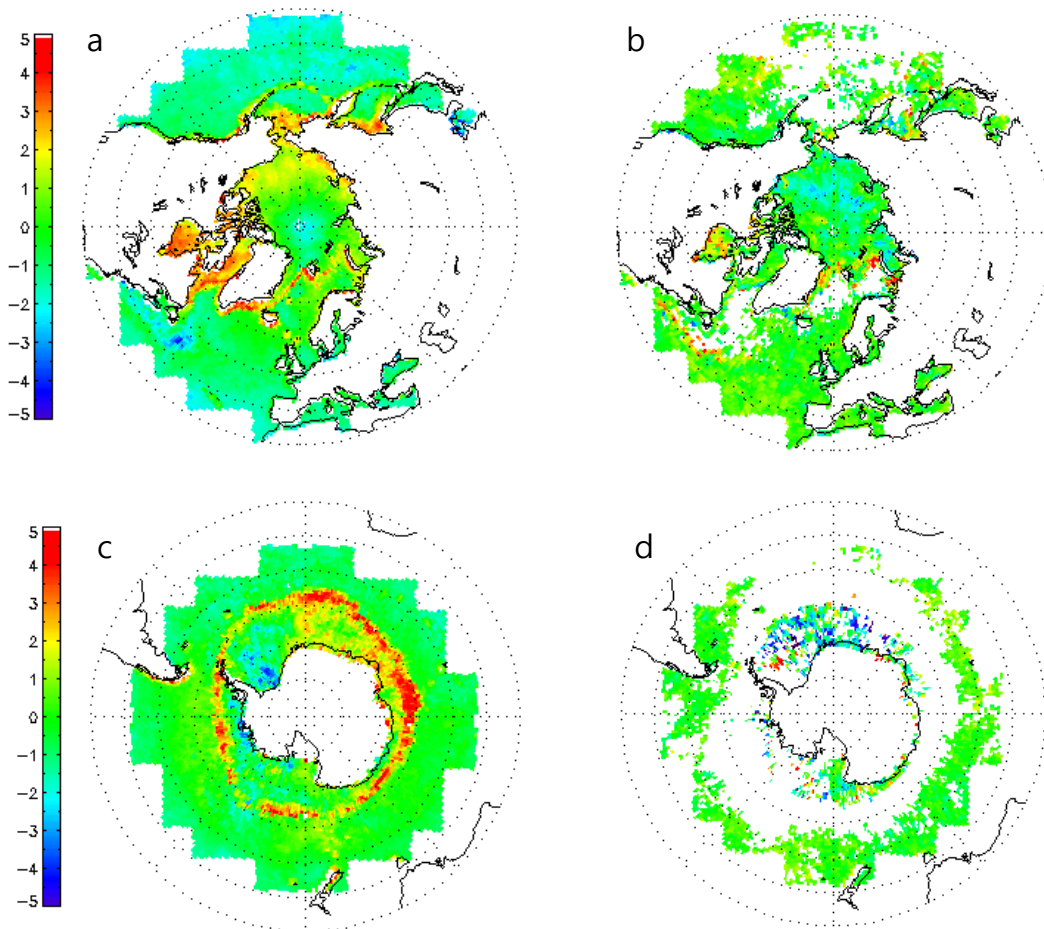
744

745 Fig. 9. Satellite-derived 9-day anomaly trends (K yr^{-1}) in a grid box of $1^\circ \times 1^\circ$ over the northern hemisphere
746 during April 16-24 of 2003-2014, for the (a) $T_{\text{skin}}(\text{MODIS})$, (c) $T_{\text{skin}}(\text{AA_V6})$, and (e) $T_{\text{skin}}(\text{AO_V6})$, and over
747 the southern hemisphere during September 16-24 of 2003-2014, for the (b) $T_{\text{skin}}(\text{MODIS})$, (d) $T_{\text{skin}}(\text{AA_V6})$,
748 and (f) $T_{\text{skin}}(\text{AO_V6})$.

749

$T_{skin}(MODIS) \text{ minus } T_{skin}(AA_V6)$

Trend difference



750

751

752

753 Fig. 10. (a) 12-year mean of $T_{skin}(MODIS) \text{ minus } T_{skin}(AA_V6)$ (K) over the northern hemisphere
754 during April 16-24 of 2003-2014, and (b) difference in the thermal trend (K/decade) between T_{skin}
755 (MODIS) and $T_{skin}(AA_V6)$. Figures 10c-d are the same as Figs.10a-b except for over the southern
756 hemisphere during September 16-24 of 2003-2014, respectively. Figure 10a is the same as Fig. 3a in
757 Kang and Yoo (2015).

758

759

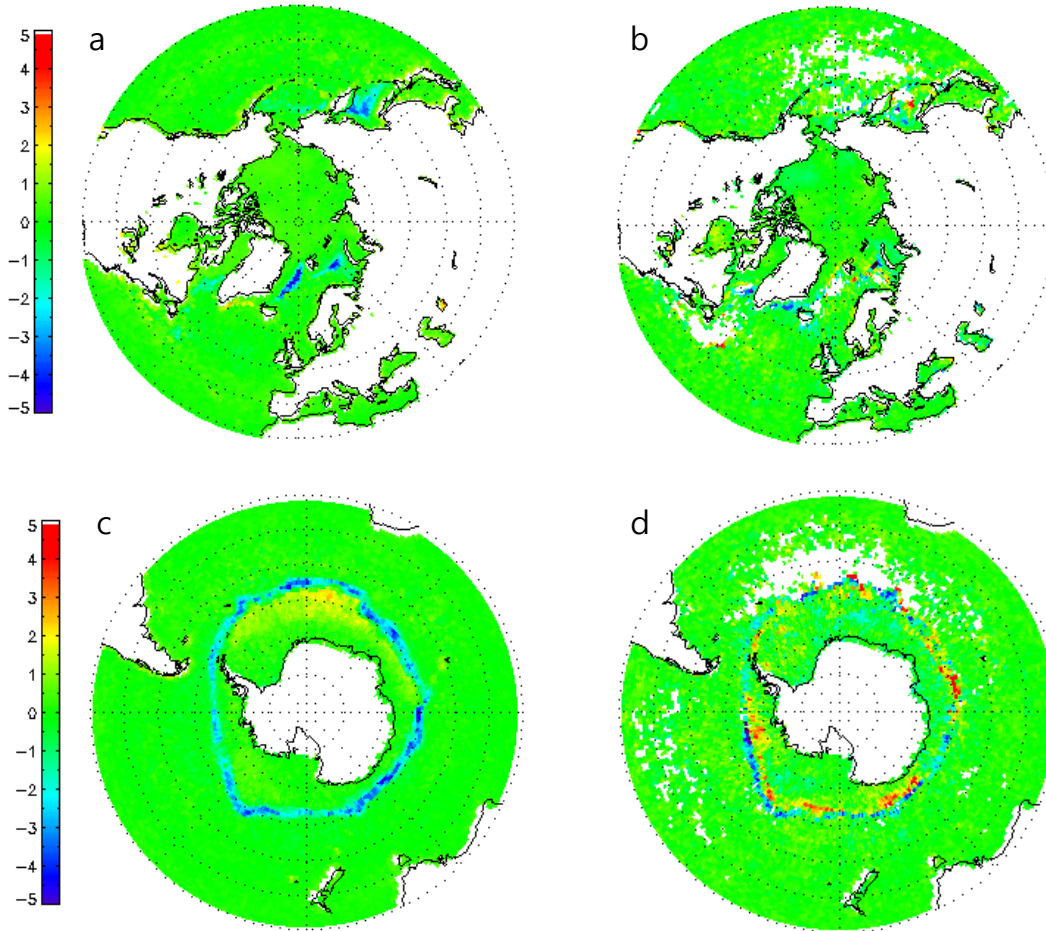
760

761

762

$T_{skin}(AO_V6)$ minus $T_{skin}(AA_V6)$

Trend difference



763

764

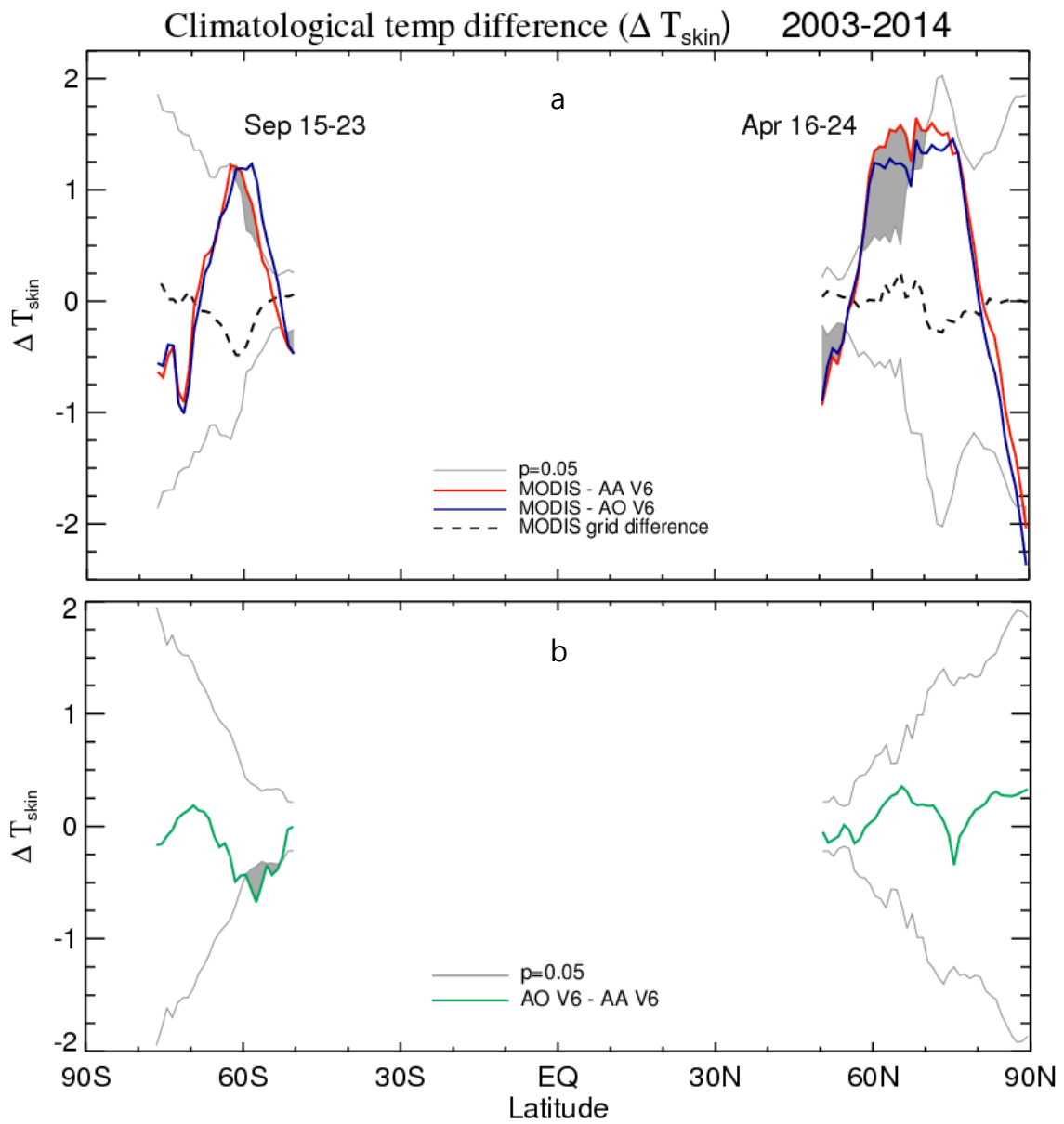
765

766 Fig. 11. Same as Fig. 10 except for $T_{skin}(AO_V6)$ minus $T_{skin}(AA_V6)$. Figure 11a is the same as Fig.
767 3c in Kang and Yoo (2015).

768

769

770



771

772 Fig. A1. The difference values (a) between T_{skin} (MODIS) and T_{skin} (AA_V6), and (b) T_{skin} (AA_V6)
 773 and T_{skin} (AO_V6) over a possibly frozen region; shown in Fig. 7. The 5% significance level is
 774 presented as grey solid lines, and the shaded areas are statistically significant at the 0.05 level.

775

776